

**Department of Physics and Astronomy  
University of Heidelberg**

Bachelor Thesis in Physics  
submitted by

**Lorenz Reinhard Luger**

born in Frankfurt am Main (Germany)

**2018**

Measurement of electrons originating from  
beauty-hadron decays in p–Pb collisions at  
 $\sqrt{s_{\text{NN}}} = 5.02 \text{ TeV}$  with the ALICE detector at the  
LHC

This Bachelor Thesis has been carried out by Lorenz Luger at the  
Physics Institute in Heidelberg  
under the supervision of  
Priv. Doz. Dr. Yvonne Chiara Pachmayer

## Abstract

In ultrarelativistic heavy-ion collisions the quark-gluon plasma (QGP), a deconfined state of quarks and gluons, is created. Partons lose energy as they traverse the QGP and this interaction with the medium can be studied using beauty-hadrons as probe. Overall goal of this analysis is to contribute to the general understanding of the QGP and its characteristics. To analyze the interaction with the medium reference measurements with p–Pb collisions, where no QGP is created, are obtained to estimate the cold nuclear matter effects. The semi-leptonic decay of beauty-hadrons was used to observe particle production as a function of  $p_T$ . This approach is based on the comparatively large decay length of beauty-hadrons ( $c\tau_B \approx 500 \mu\text{m}$ ). From the inclusive electron yield the background sources were subtracted by a cocktail approach and the raw  $p_T$  spectrum was obtained in mid-rapidity minimum-bias p–Pb collisions at  $\sqrt{s_{\text{NN}}} = 5.02 \text{ TeV}$ .

## Kurzfassung

In Kollisionen von ultrarelativistischen Schwerionen entsteht das Quark-Gluon-Plasma (QGP), ein Zustand in welchem das Confinement der Quarks und Gluonen aufgehoben ist. Partonen, welche das Medium passieren, interagieren damit und verlieren dabei Energie. Um diese Interaktion zu charakterisieren haben sich Beauty-Hadrons bewährt. Übergeordnetes Ziel dieser Analyse ist die Akquisition von Wissen über das QGP und seine Eigenschaften. Dabei sind Referenzmessungen notwendig, um Effekte abzuschätzen, die alleine aus der Interaktion von p–Pb stammen, also aufgrund von kalter, nuklearer Materie auftreten und nicht auf die Entstehung des QGP zurückzuführen sind. Der semi-leptonische Beauty-Hadron Zerfall wurde verwendet um Erkenntnisse über die Teilchenproduktion als Funktion von  $p_T$  zu erlangen. Dieser Ansatz basiert auf der vergleichsweise lange Zerfallslänge von Beauty-Hadronen ( $c\tau_B \approx 500 \mu\text{m}$ ). Mit Hilfe einer sogenannten Cocktail-Methode wurden sämtliche Untergrundquellen vom inklusiven Elektronenspektrum entfernt und das unkorrigierte  $p_T$  Spektrum von Elektronen aus Beauty-Hadron Zerfällen bei mittlerer Rapidität und minimalem Bias in p–Pb Kollisionen mit einer Schwerpunktsenergie von  $\sqrt{s_{\text{NN}}} = 5.02 \text{ TeV}$  wurde bestimmt.

# Contents

<b>1</b>	<b>Introduction</b>	<b>1</b>
<b>2</b>	<b>Analysis strategy</b>	<b>8</b>
<b>3</b>	<b>A Large Ion Collider Experiment</b>	<b>10</b>
3.1	Time-Of-Flight detector . . . . .	11
3.2	Time Projection Chamber . . . . .	12
3.3	Inner Tracking System . . . . .	12
3.4	V0 detector . . . . .	13
<b>4</b>	<b>Track and event selection</b>	<b>14</b>
4.1	Data . . . . .	14
4.2	Monte Carlo simulation . . . . .	14
4.3	Track selection . . . . .	14
4.4	Event selection . . . . .	15
<b>5</b>	<b>Electron identification</b>	<b>16</b>
5.1	Electron identification with the TOF detector . . . . .	16
5.2	Electron identification with the TPC detector . . . . .	19
5.2.1	Momentum dependence . . . . .	20
5.2.2	Pseudorapidity dependence . . . . .	25
5.2.3	Electrons per event . . . . .	26
5.3	Summary for eID . . . . .	27
<b>6</b>	<b>Impact parameter distribution</b>	<b>28</b>
6.1	Momentum dependence . . . . .	28
6.2	Angular dependence . . . . .	32
6.3	Conclusion and impact parameter cut . . . . .	33
<b>7</b>	<b>Electron background</b>	<b>34</b>
7.1	Subtraction of the background sources . . . . .	35
<b>8</b>	<b>Discussion, summary and outlook</b>	<b>39</b>
<b>9</b>	<b>Appendix</b>	<b>40</b>
<b>10</b>	<b>Acknowledgment</b>	<b>50</b>

# 1 Introduction

One of the largest research areas for physicists is quantum chromodynamics (QCD) which is the theory of particles interacting via the strong force. These particles are quarks and gluons which do not exist as free particles in nature but are bound in color neutral hadrons. Quarks carry color charge while antiquarks carry anticolor charge. The exchange particles of the strong interaction are gluons which carry color and anticolor as well. Coming from group theory 9 different combinations of color and anticolor exist for gluons, where 8 of them contribute to the strong interaction [12]. Thus color charged gluons interact with themselves. Furthermore, QCD is based on the SU(3) gauge group.

From quantum electrodynamics (QED) it is known that particles of opposite charge are not always influenced by the complete charge of the other one, since e.g. a single electron charge in vacuum creates dipole pairs, such as  $e^+e^-$ -pairs, surrounding it. If the distance between the electron (particle one) and the incoming charge carrier (particle two) is large enough, a shield occurs resulting in a smaller charge of particle two in the potential of particle one [12]. This is called vacuum polarization. For the strong interaction there is not only the contribution of the just explained “fermion-loop shield” but also the “gluon-loop antishield” coming from the selfinteraction of the gluons [12]. Therefore the coupling constant of the strong interaction  $\alpha_s$  decreases with increasing momentum transfer, which is equivalent to decreasing distance between the interacting particles. This behavior, which is opposite to that of the QED constant, can be seen in Fig. 1. This phenomenon is called asymptotic freedom because for high  $Q^2$  ( $Q^2 \rightarrow \infty$ )  $\alpha_s$  decreases ( $\alpha_s \rightarrow 0$ ). Quarks and gluons build bound color neutral hadronic states (confinement) and cannot be observed isolated under normal conditions. ”Within the hadron, the strong interaction affects them comparatively little, but strongly confines them within a small volume.” [13]. But for high energy densities (little less than  $1 \text{ GeVfm}^{-3}$ ) quarks and gluons are set free and deconfinement is created [29].

In Fig. 2 the potential of the strong interaction is plotted which is approximated by the following equation:

$$V_{\text{QCD}}(r) = -\frac{4}{3} \frac{\alpha_s}{r} + kr \quad (1)$$

The first part of this equation describes the attractive interaction while the second one describes the creation of quark-antiquark pairs due to increasing potential for larger distances ( $\sim \text{fm}$ ). This second part is originating from virtual gluon exchange between two quarks, where a color field with a tube like character with constant energy density exists. In other words the field lines attract each other due to the self-interaction of the gluons. Furthermore, the hypothetical energy to divide two quarks would be infinite. The color energy created by the strong potential becomes already big enough to create new quark-antiquark pairs when pulling apart the quarks at distances larger than 1–2 fm leading to new color neutral hadrons.

Quarks in hadronic states have to be divided into valence- and sea quarks. Valence quarks are the quarks that define the attributes such as mass, spin, charge and momentum of a hadronic state while sea quarks are virtual quark-antiquark pairs

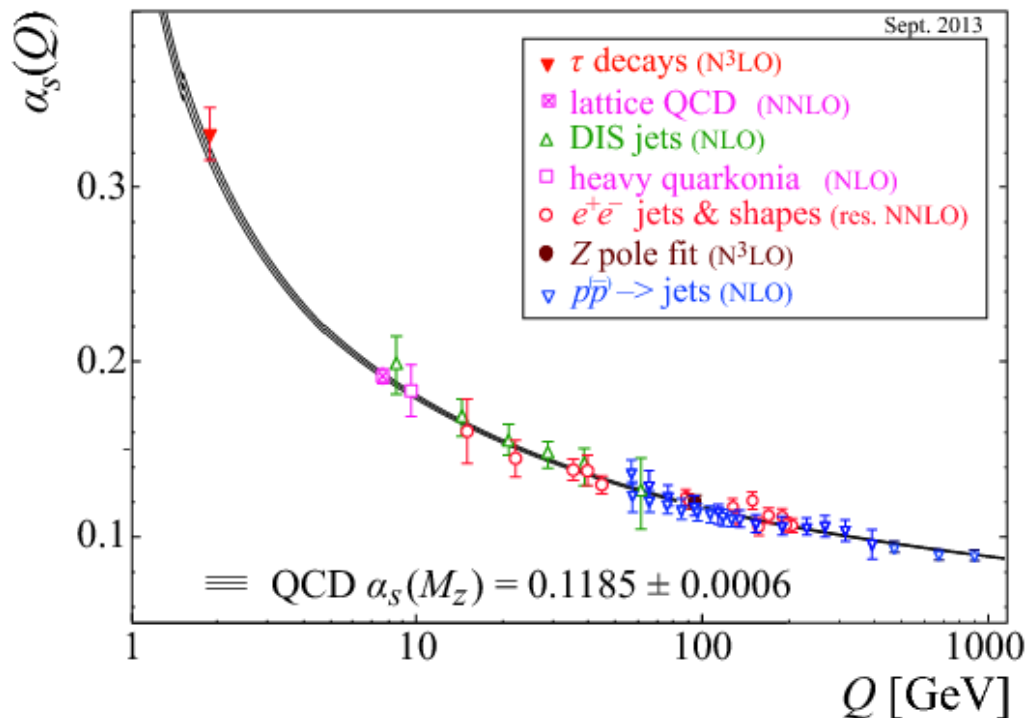


Figure 1: Energy dependence of the coupling constant of the strong interaction [27].

created by the radiation of a gluon resulting in pair production near a valence quark and surrounding it like a sea [30]. This is mainly important for deep inelastic scattering, especially with small Bjorken- $x$ .

Hadronic states can be divided into two groups of color neutral particles which are mesons and baryons. Mesons consist of quarks and antiquarks where one quark carries a certain color which is annihilated by the corresponding anticolor of the antiquark. Baryons contain 3 constituents of quarks where each quark carries a different color than the others. Therefore the colors cancel each other out and a bound color neutral state is obtained. For both, mesons and baryons, exist corresponding antiparticles. Since quarks and antiquarks carry half-integer spin, mesons carry integer spin while baryons carry half-integer spin. The mass of the hadronic states depends not only on the mass of the constituents but the spin wave function, the contribution from gluon interaction and, most of all, on chiral symmetry breaking. In total, this leads to a mass much higher than that of the valence quarks.

Deconfinement and confinement are two of the keywords from the above paragraphs. They describe whether quarks occur as free particles or in a bound hadronic state. Between these two states a phase transition is expected. To obtain this transition very extreme conditions of temperatures and energy densities compared to normal nuclear matter have to be fulfilled.

After the Big Bang the universe was so dense that pressure and temperature were so high that the quark-gluon plasma (QGP) was formed (see Fig. 3). The baryochemical potential  $\mu_B$  describes how much energy is necessary to add a baryon (e.g. neutron or proton) to the system, in other words: it indicates the imbalance

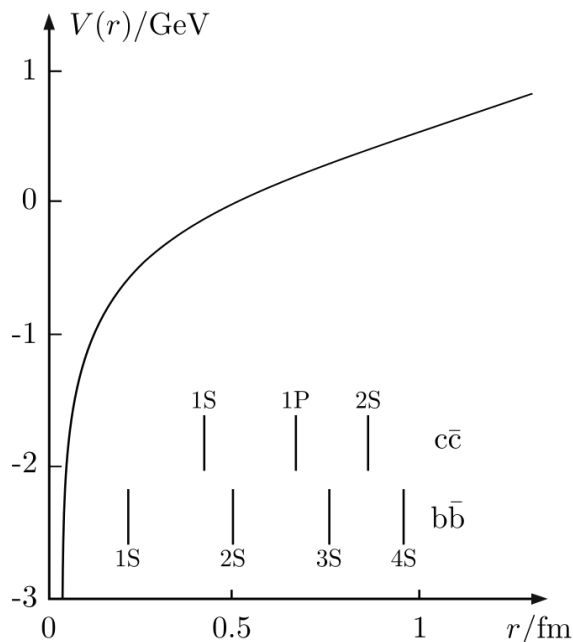


Figure 2: Potential of the strong interaction in dependence of the distance between quark and antiquark with average radii of various quarkonia as comparison[28].

between matter and antimatter and is zero for perfect balance [31] which was approximately the case for the Big Bang. QGP can also be created by ultra relativistic heavy ion beam collisions because high enough temperature and energy density are fulfilled. Heavy ions are necessary because when the beams collide each nucleon inside the corresponding nucleus collides with a multitude of nucleons which fulfills the QGP conditions. Since we live in a world consisting of matter the baryochemical potential is positive nowadays, which leads to differences in the ratio of initial number of baryons to the final one between the formation of the QGP created by the Big Bang and the QGP created by ultrarelativistic heavy ion beam collisions [10]. In the QGP deconfinement is present. Thus, quarks and gluons appear as free particles.

For deeper understanding of the QGP heavy ion collisions are performed to recreate the QGP and obtain information about it by measuring final state particles coming from the collisions. Heavy ion beams ( $A_{Pb} = 208$ ) are accelerated close to the speed of light and then a collision between both beams is forced. Due to the ultrarelativistic speed of the ion beams the ions become strongly Lorentz contracted and pancake shaped before the collision. This whole process can be spectated in Fig. 4. After about  $\tau \approx 1 \text{ fm}/c$  the QGP is created. For this, the critical temperature  $T_c$  of 156 MeV has to be exceeded [10]. Because of a very high density gradient compared to the surrounding, the QGP expands very quickly and therefore cools off which leads to a very small lifetime of  $\tau \approx 10 \text{ fm}/c$  [10]. In other words the energy density decreases. After dropping under the chemical freeze-out temperature ( $T_{ch} \approx T_c$ ), which means that the particle composition of the matter ceases to change [13], hadronic freeze out begins. Quarks and gluons start to build hadronic states and the QGP absolves a phase transition into the hadron gas (HG).

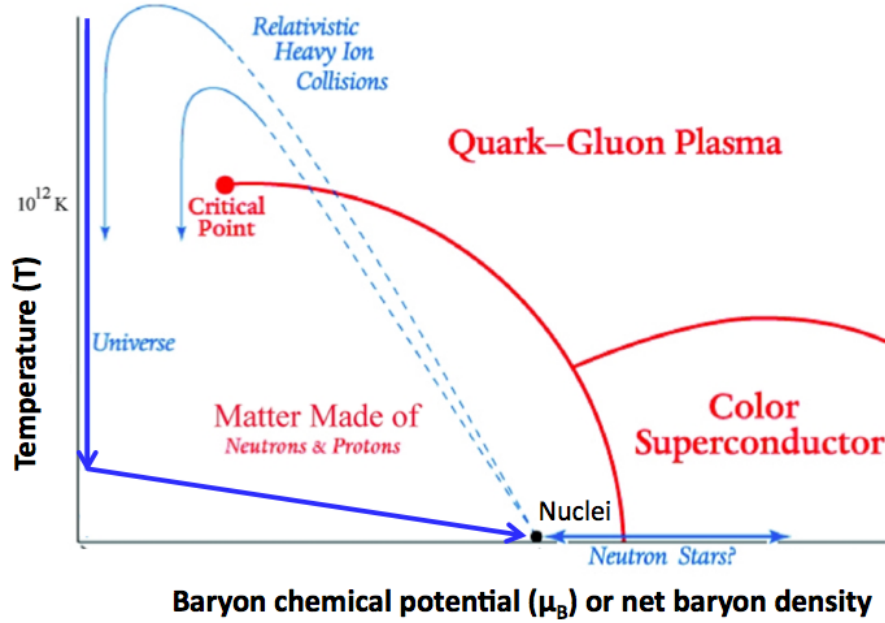


Figure 3: Phasediagramm of QCD [11].

This whole process is visualized in Fig. 4. In the HG, for temperatures below the kinetic freeze-out, hadron momenta stabilize for distances too large for hadrons to interact because no inelastic processes occur anymore.

To understand the properties of the QGP and how it influences particle production is one of the main targets of nowadays physicists. As pointed out earlier, the dominant part of the hadron mass is caused by chiral symmetry breaking. In the QGP chiral symmetry becomes recovered again [13]. Since there is no symmetry breaking for heavy quarks, which means that higgs mass and QCD mass do not differ [32], this is not important for heavy quarks.

Partons passing through the QGP loose energy i.e. via radiation or collisional processes. This energy loss depends on various variables such as distance traversed inside the QGP, medium density, quark mass and color charge (Casimir factor) [33] [27]. Thus, heavy-flavored quarks, which are quarks such as beauty (b) or charm (c), loose less energy in the QGP but much less than gluons:  $\Delta E_b < \Delta E_c < \Delta E_{\text{gluon}}$ . Therefore the energy loss of high energy partons in the QGP ( $\text{QCD}_{\text{medium}}$ ) is an interesting property because it characterizes the strength of the interaction. Since it is not possible to observe the quarks directly, the influence of the QGP medium has to be extracted from the measured hadrons created in the hadronic freeze-out by the influenced quarks. It is compared to a measurement where no QGP is created (e.g. p–Pb and pp) to determine the energy loss caused only by the interaction with the medium [13]. The interaction with the medium leads to a suppression of particle production at large transverse momenta compared to the corresponding measurement in pp collisions. Therefore the nuclear modification factor is an excellent property to compare the behavior of partons in the  $\text{QCD}_{\text{medium}}$  to that of  $\text{QCD}_{\text{vacuum}}$  by comparing the nuclear modification factor of the respective

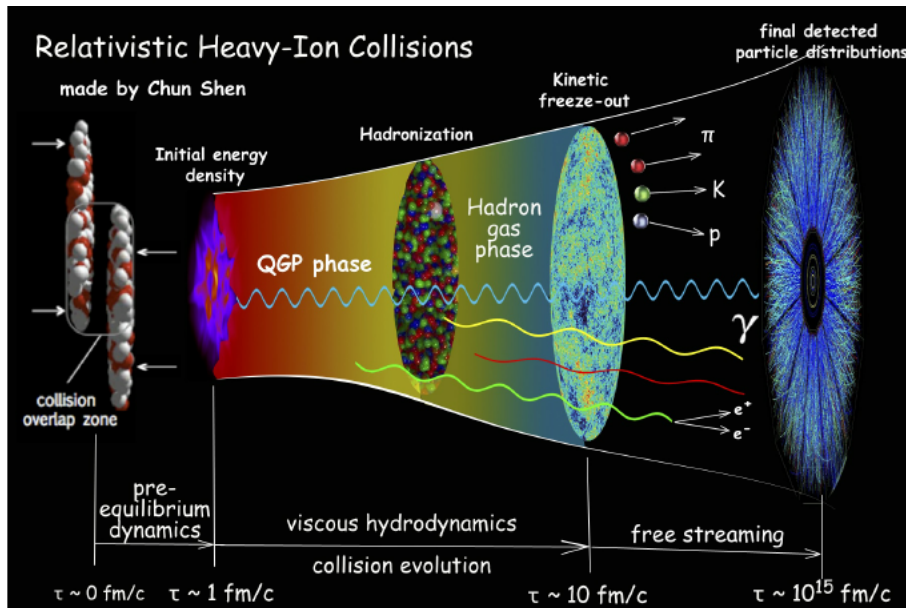


Figure 4: Evolution of the colliding beam particles[14].

measured hadron. Concrete, the yield of a given particle is measured as a function of  $p_T$  in heavy-ion collision and compared to that of a corresponding superposition of many independent nucleon-nucleon collisions. If the yields are equal the nuclear modification factor is unity. In the following equation the expected number of binary collisions is described by  $\langle N_{\text{coll}} \rangle$ .

$$R_{AA} = \frac{dN_{AA}/dp_T}{\langle N_{\text{coll}} \rangle dN_{pp}/dp_T} \propto \frac{\text{QCD}_{\text{medium}}}{\text{QCD}_{\text{vacuum}}} \quad (2)$$

Thus, in case this ratio is unity the QGP does not effect particle production. As pointed out above, the energy loss of partons varies among quarks and gluons which leads to different nuclear modification factors since the repective energy loss in the  $\text{QCD}_{\text{medium}}$  is strongly differing. Thus, the suppression differs in strength and leads to the following expected hierarchy:  $R_{AA}^b > R_{AA}^c > R_{AA}^{\text{gluon}}$  [33].

This analysis focuses on particles which contain a beauty-quark or antiquark. Heavy-flavored hadrons are qualified for analyses of the QGP because heavy quarks are generated more quickly ( $< 0.1 \text{ fm}/c$  [3]) than the QGP ( $\approx 0.3 \text{ fm}/c$  [3]) and are therefore sensitive towards the complete temporal and spatial evolution of the QGP. Furthermore the flavor composition of beauty-quarks and antiquarks is approximately constant inside the QGP due to two characteristics. The temperature of the QGP of about 156 MeV corresponds to a mass larger than light quarks such as strange, up and down quark. Therefore they can be created in quark antiquark pairs in the  $\text{QCD}_{\text{medium}}$  due to the high temperature [34]. Thus, first characteristic of the beauty-quarks is the high mass of  $4.2 \text{ GeV}/c^2$  which is much heavier than the mass which corresponds to the temperature of the QGP. Second characteristic is the small amount of pair annihilation due to the small number density of beauty-quark and antiquark.

In addition, because of the high mass of the beauty-quark compared to  $\Lambda_{\text{QCD}} \approx 218$  MeV which is called the QCD mass scale, theoretical methods for cross section calculations (perturbativ methods) can be applied to calculate the cross section theoretically [35].

At the LHC pp, Pb–Pb and p–Pb collision systems are measured. These 3 different collisions have to be considered because they correspond to different scenarios. The main focus of the ALICE experiment is to examine central Pb–Pb collisions because they create the QGP. For a comparison of  $\text{QCD}_{\text{medium}}$  to  $\text{QCD}_{\text{vacuum}}$  PP collisions are studied where it is assumed that no QGP is formed. A direct comparison neglects the cold nuclear matter (CNM) effects which are estimated by p–Pb collisions. In this collision setup it is also assumed that no QGP is formed. The CNM effects can be for example a modification of the parton distribution function (PDF) in a nucleus compared to that of a free proton [3] or multiple scattering inside the nucleus ( $k_T$ -broadening) which can change the resulting heavy-flavor hadron momentum spectrum [15]. Thus, they have to be considered for an interpretation of the  $R_{\text{AA}}$  [2]. Since the nuclear modification factor varies with different center-of-mass (CMS) energy, collision system,  $p_T$ , centrality and pseudorapidity differential analyses have to be performed.

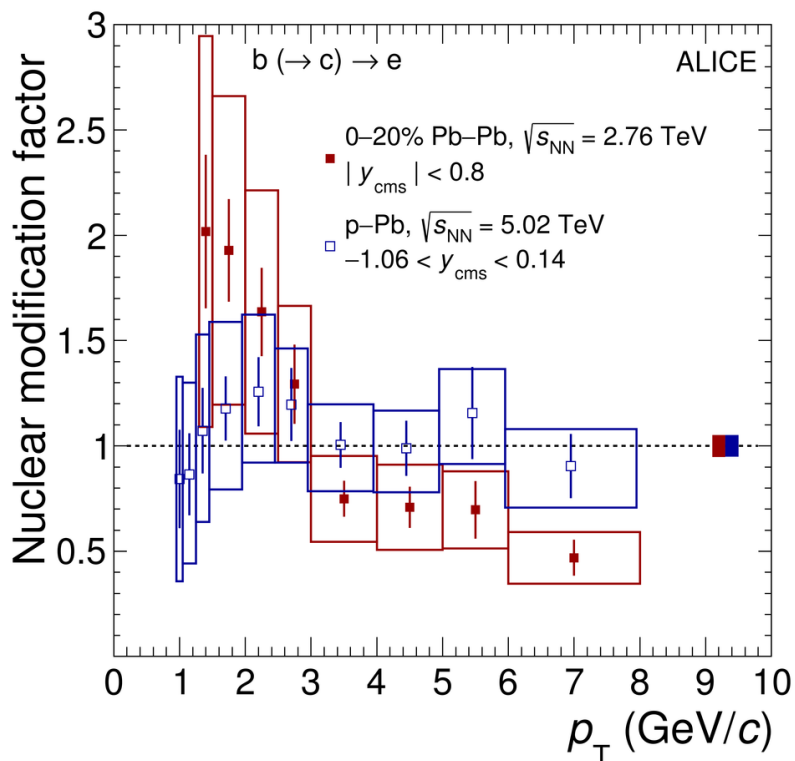


Figure 5: Nuclear modification factor of electrons from beauty-hadron decays in p–Pb and Pb–Pb collisions [4].

Figure 5 shows the nuclear modification factor in central Pb–Pb collisions at mid-rapidity with a center-of-mass energy of  $\sqrt{s_{\text{NN}}} = 2.76$  TeV and in p–Pb with a

center-of-mass energy of  $\sqrt{s_{\text{NN}}} = 5.02$  TeV. The nuclear modification factor was obtained by using the semi leptonic decay of  $B$ -hadrons including the indirect decay of  $B \rightarrow D \rightarrow e$ . Due to the presence of the QGP suppression is visible at high  $p_{\text{T}}$  e.g. at 7 GeV/ $c$  where the nuclear modification factors deviate about 0.5 because of the proclaimed energy loss of beauty-quarks in the QGP.

In this thesis electrons coming from the semi-leptonic decay of  $B$ -hadrons generated in p-Pb collisions with a center-of-mass energy of  $\sqrt{s_{\text{NN}}} = 5.02$  TeV are studied. At first the analysis strategy will be explained in Chapter 2 and why the semi-leptonic decays of  $B$ -mesons are suitable to examine the QGP. This will be followed by Chapter 3 where for this thesis important sub-detectors of the ALICE detector will be explained. Details of the analysis, such as track - and event selection, as well as the Monte Carlo and data sample will be described in Chapter 4. Topic of the 5<sup>th</sup> Chapter is the electron and positron identification. In the 6<sup>th</sup> Chapter the impact parameter distribution will be analyzed. After this the background distribution and subtraction will be discussed in Chapter 7. Chapter 8 will be a general discussion of all outpointed results as well as a summary and outlook.

## 2 Analysis strategy

Since the QGP cools down and hadronic freeze-out starts to occur, only hadronic states are left. Hadronic states containing a heavy quarks, for example  $D$ - or  $B$ -mesons, have a lifetime (decay length) of e.g.  $c\tau_{B^\pm} \approx 490 \mu\text{m}$ ,  $c\tau_{B^0} \approx 460 \mu\text{m}$  [5] and  $c\tau_{D^0} \approx 120 \mu\text{m}$ ,  $c\tau_{D^\pm} \approx 310 \mu\text{m}$  [6]. Since this time is short compared to the necessary for a particle to reach the detectors (“free streaming” in Fig. 4), the hadrons cannot directly be measured by the ALICE detector. Therefore decay products with a longer lifetime and high enough appearance, which are measurable for our experimental setup, have to be considered. The resulting decay product has to fulfill different criteria which are lifetime, tractability and distinctness.

Charged particles such as electrons or positrons (leptons) are therefore good candidates because sub-detectors of the ALICE experiment such as the Time-of-Flight detector (TOF) and the Time-Projection-Chamber (TPC) can reconstruct the path of charged particles with extreme high precision and will provide particle identification (PID) which will be further explained in Chapter 3. Theoretically, hadronic decay modes of the  $B$ -hadrons could also be used for analysis but for this, the branching ratios of the different decays have to be multiplied which leads to a much weaker signal compared to the semi-leptonic approach [13]. The term electron will be used for both electrons and positrons in the whole thesis. Electrons from  $B$ -hadron decays originate either from direct decays ( $b \rightarrow e \approx 11\%$ ) or from cascade decays ( $b \rightarrow c \rightarrow e \approx 10\%$ ) [3]. Consequently, an advantage of a semi-leptonic approach is that there is a high amount of detectable particles created by the beauty-decay ( $b \rightarrow e \approx 20,5\%$  probability) and the low  $p_T$  reach [13] [3].

For different decay sources electrons have different impact parameter distributions. This parameter is defined as the closest perpendicular distance between reconstructed trajectory of the spectated particle towards the primary vertex and is often referred to as Distance of Closest Approach (DCA). Electrons originating from  $B$ -mesons have a larger impact parameter distribution compared to other electron sources because the DCA depends on the decay length of the mother particle which is larger for beauty-hadrons [13].

In Fig. 6, the impact parameter distributions for electrons originating from different decays are shown. Due to the sizable decay length of beauty-hadrons the DCA distribution of the corresponding electrons is comparatively large followed by the one of electrons from semi-leptonic decays of charm-hadrons. Furthermore, the DCA distributions of electron background sources such as electrons coming from photon conversion inside the detector material [13] or electrons coming from Dalitz decays can also be seen in Fig. 6. Further details will be explained in Chapter 7. In Fig. 6 are also the impact parameter cuts sketched which were used in the analysis [36].

By applying cuts on the impact parameter, the signal-to-background ratio (S/B) between electrons originating from beauty-hadron decays compared to the rest (background) can be optimized. Thus, after cuts, only left and right tail of the impact parameter distribution are used for further analysis since the S/B is best for large DCA. Then the contribution of the electron background can be estimated by

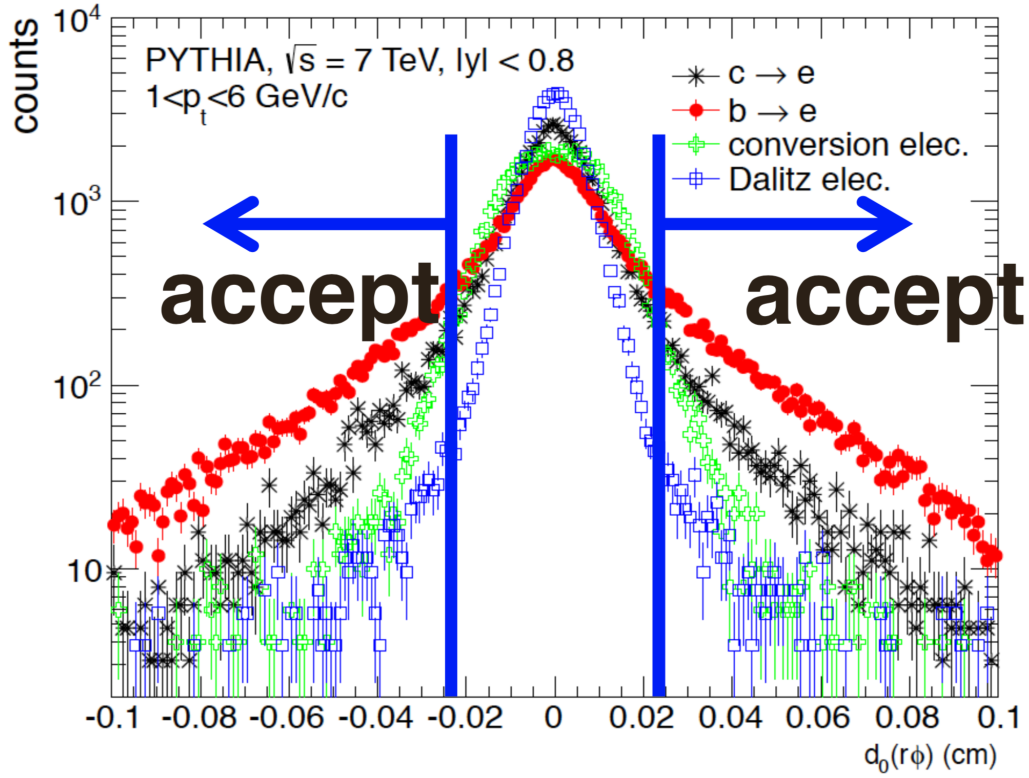


Figure 6: Impact parameter distributions for electrons from various decays in  $\sqrt{s}=7$  TeV pp collisions with PYTHIA for  $|y| < 0.8$  and  $1 < p_T < 6$  GeV/c with sketched DCA cut [36].

other ALICE measurements and subtracted from the inclusive electron spectrum. On one hand the signal-to-background ratio increases for very large impact parameters but on the other hand there are fewer electrons at large impact parameter. Thus, a cut has to be applied where the signal is not too sensitive towards statistical fluctuations and the S/B is good.

This kind of analysis was already performed for data from 2013 but the data from 2016 has  $\approx 2.4$  as much events as in 2013 to increase the signal for larger impact parameter [3].

### 3 A Large Ion Collider Experiment

The ALICE detector is used for studies of heavy-ion collisions in order to analyze the QGP and its characteristics as well as its influence on particle production. Particle identification (PID), primary and secondary vertexing and tracking at a large transverse momentum range ( $100 \text{ MeV}/c \leq p_T \leq 100 \text{ GeV}/c$ ) are the main purposes of the detector. The good momentum resolution of the order of 3 % for  $p_T = 40 \text{ GeV}/c$  can be derived from [16]. For lower momentum the resolution decreases (improves). The general composition of the ALICE detector, consisting of a muon arm at forward rapidity and a central barrel at mid-rapidity, is shown in Fig. 7. Furthermore, the central barrel consists of different detector layers around the nominal collision point. A solenoid magnet which encloses the detector system (object number 10 in Fig. 7) generates a field of 0.5 T parallel to the beam. Imperative for the whole system is the right-handed Cartesian coordinate system which has its origin at the nominal interaction point (IP). Perpendicular to the  $z$ -axis, which is parallel to the beam direction and has negative values in direction of the muon arm, are the  $x$ - and  $y$ -axis. While the  $x$ -direction points towards the accelerator center, the  $y$ -axis is aligned upwards. Two angles are defined around the interaction point. On the one hand is the azimuthal angle  $\phi$  which increases counter clockwise from the  $x$ -axis (on the  $x$ -axis:  $\phi = 0$ ) to the  $y$ -axis (on the  $y$ -axis:  $\phi = \pi/2$ ). On the other hand is the polar angle  $\theta$  which increases from the  $z$ -axis (where  $\theta = 0$ ) to the  $x, y$  plane (where  $\theta = \pi/2$ ). For this and additional information see [18]. Details of the ALICE detector and its performance can be found in [16] and [8].

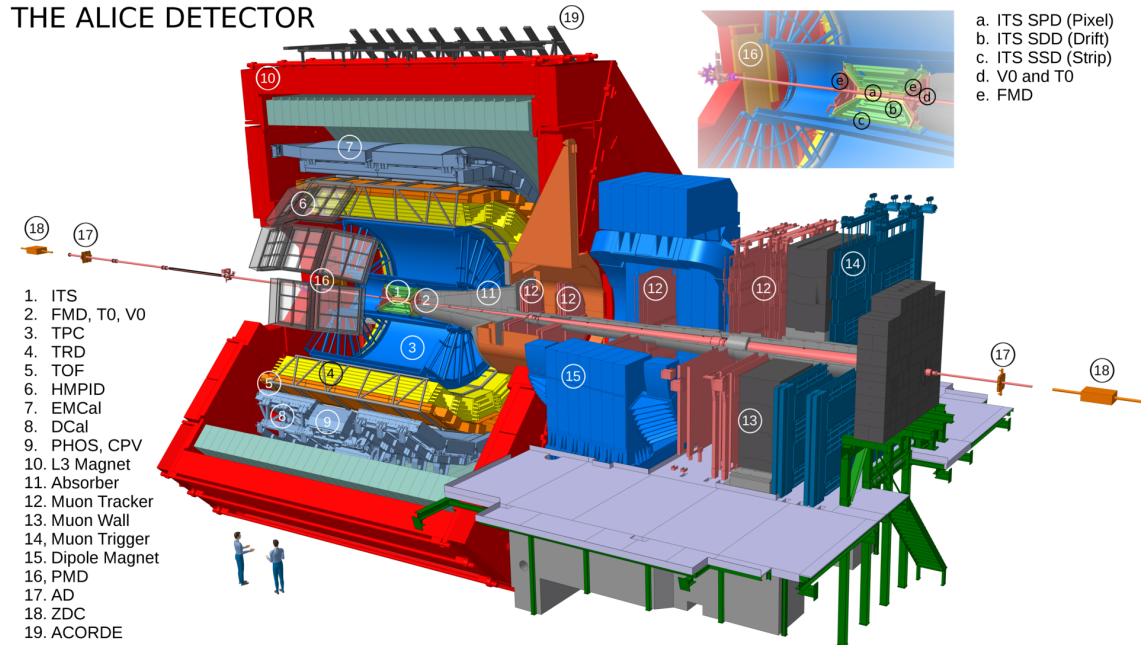


Figure 7: The ALICE detector and its subsystems [8].

The inner most detector is the Inner Tracking System (ITS, number 1 in Fig. 7) which is mainly used for reconstruction of the primary vertex and secondary vertices and is therefore situated closest to the nominal collision point. It consists of multiple

layers which can be seen in the right upper edge of Fig. 7. It is surrounded by the Time Projection Chamber (TPC, number 3 in Fig. 7) which has the main purpose to determine the energy loss and the trajectory of charged particles. Wrapped around the TPC is the Transition Radiation Detector (TRD, number 4 in Fig. 7) which can be used to separate electrons from other charged particles. The next outer layer is the Time-of-Flight (TOF) detector (number 5 in Fig. 7) that measures the time-of-flight. Furthest from the interaction point are the three calorimeters HMPID, EMCal and DCal (number 7, 8, 9 in Fig. 7). Various detectors used e.g. for triggering are installed close to the beam pipe. The event selection will be described in the next chapter while in this chapter the detectors relevant for this thesis will be discussed.

### 3.1 Time-Of-Flight detector

The time-of-flight detector (TOF), already mentioned above, is positioned in a distance of about 3.7 m from the nominal interaction point and can measure charged particles in a rapidity range of  $|y| < 0.9$  and azimuthal range of  $2\pi$ . The detected observable is the time a particle needs from the interaction point to the TOF [8]. The velocity  $\beta$  of the charged particles can be calculated from this (see [8]). For this, a very precise time resolution is necessary which is fulfilled by the detector by usage of multigap resistive plates. Combining scintillators for the start time measurement ( $t_0$ ) with a time resolution  $< 80$  ps and the resistive plate chambers (RPC) of the TOF detector for a measurement of the arrival time ( $t_1$ ) with a time resolution of  $< 40$  ps leads to a total resolution of  $\sigma_{\text{TOF}}^2 = \sigma_{t_0}^2 + \sigma_{t_1}^2$  about  $\sigma_{\text{TOF}} < 90$  ps. With information such as track length  $L$  and momentum  $p$  provided by the tracking detectors ITS and TPC, the mass of the particle can be calculated via the following equation taken from [20]:

$$m = \frac{p}{c} \sqrt{\frac{t^2 c^2}{L^2} - 1} \quad (3)$$

In addition to that, the TOF can distinguish between different relativistic particles with the same momentum  $p$  by comparing different hypotheses with a corresponding time difference  $\Delta t$  which is defined in [20] as:

$$\Delta t \approx \frac{Lc}{2p^2} \cdot (m_1^2 - m_2^2) \quad (4)$$

Dividing this value by the time resolution leads to an interesting and often used observable:

$$N_{\sigma_{\text{electron}}^{\text{TOF}}} = \frac{\Delta t | e}{\sigma_{\text{TOF}}} = \frac{t_{\text{measured}} - t_{\text{expected}} | e}{\sigma_{\text{TOF}}} \quad (5)$$

which expresses the deviation in time taken by the measured particle to the expected values for the electron hypothesis in units of the detector resolution  $\sigma_{\text{TOF}}$  [3]. How this is used for electron identification is explained in Chapter 5.1.

### 3.2 Time Projection Chamber

For reconstruction of particle tracks the time projection chamber (TPC) is used. It is a cylindrical gas chamber with an extent of 5m length and diameter measuring charged particles in a rapidity range of  $|y| < 0.9$  and azimuthal range of  $2\pi$ . In the center of the TPC is the central electrode which divides the TPC into 2 drift regions. At top and bottom of the cylindrical chamber are the readout chambers which are divided into 159 pad rows [38]. This gas is a mixture consisting of 90 % Ar and 10 % CO<sub>2</sub>, which becomes ionized by passing charged particles along their track [42]. The primary electrons from the ionisation process, called drift electrons, then drift along a strong electric field (400 V/cm) towards the readout chambers in the end plates. A gating grid is used to separate the drift volume and the avalanche volume where an avalanche process occurs [39]. In this process, the drift electrons collide with multiple gas atoms releasing additional drift electrons leading to a chain reaction where more and more drift electrons are released. This chain reaction is called avalanche process [39]. Separation of the 2 regions is necessary to prevent drift electrons from unwanted events of entering the avalanche region and to prevent the ion cores of drifting towards the central electrode and the drift volume. Electrons that enter the avalanche region reach the readout chambers where the signal is amplified and measured. The energy loss of the respective charged particle corresponds to the amplified signal because the energy deposit of the charged particle is proportional to the amount of free electrons which is proportional to the amplified signal. Two space coordinates can be reconstructed by the projection of the track on the pad plane. The third one is then calculated by the time-of-flight and the driftvelocity of the electrons [9]. The momentum of the particle can be calculated from the radius of the curvature and the trace since the magnetic field is known and the unknown charged particle was under influence of the Lorentz force. With information about the average specific ionisation energy loss and the momentum, the mass of the respective particle and therefore the particle species can be identified via the Bethe-Bloch-Formula. The energy loss resolution depends on several parameters such as e.g. the energy loss, pseudorapidity and track density inside the detector and is approximately 5.5 % for low and 6.8 % for high multiplicity [24]. Furthermore, an analog variable to  $N_{\sigma_{\text{electron}}^{\text{TOF}}}$  exists for the TPC which compares the energy loss of a particle to the expected one for a certain particle species (in units of the detector resolution) and is called  $N_{\sigma_{\text{electron}}^{\text{TPC}}}$  [3]. Since this work focuses on electrons the expected average energy loss corresponds to an electron hypothesis:

$$N_{\sigma_{\text{electron}}^{\text{TPC}}} = \frac{(\text{d}E/\text{d}x)_{\text{measured}} - (\text{d}E/\text{d}x)_{\text{expected}}}{\sigma(\text{d}E/\text{d}x)} | e \quad (6)$$

How this can be used for electron identification is explained in Chapter 5.2.1.

### 3.3 Inner Tracking System

This detector consists of 6 silicon detector layers where the two outermost layers are the Silicon Strip Detectors (SSD), the two middle layers are the Silicon Drift Detectors (SDD) and the innermost layers are the two Silicon Pixel Detectors (SPD).

They are positioned around the beam pipe at the collision point and will be referred to as Inner Tracking System (ITS) layers. Target of the ITS is to measure with high precision the position of the primary vertex and the closest distance of a certain track to the primary vertex in the plane transverse to the beam direction[38]. Furthermore the vertices of secondary decays can be determined. Within a range of  $2\pi$  in azimuthal angle and  $|\eta| < 0.9$  in pseudorapidity charged particles can be detected with the ITS. The DCA is separated into 2 dimensions which are  $d_{xy}$  and  $d_z$ . The DCA has to be obtained since the track of a particle does not suffice to determine the secondary vertex.

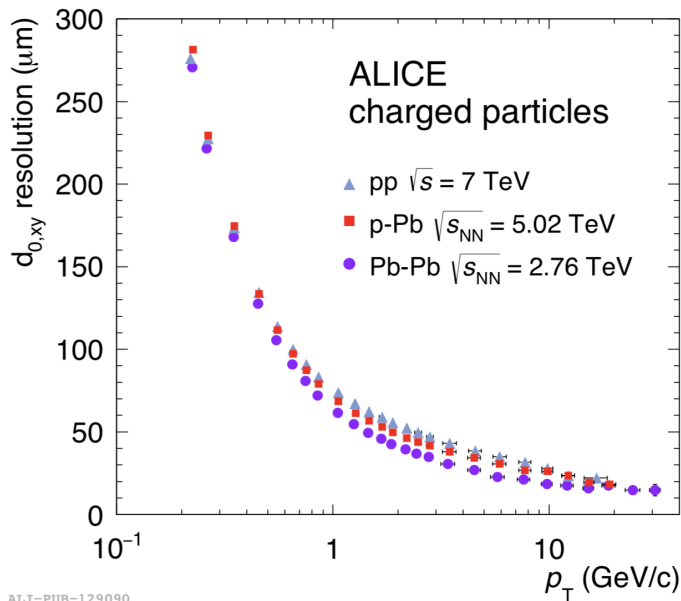


Figure 8: Impact parameter resolution for the  $xy$ -plane in dependency of the transverse momentum for various collision scenarios [8].

In Fig. 8 the resolution of  $d_{xy}$  (denoted as  $d_{0,xy}$  in Fig. 8) for different collision scenarios is shown as a function of the transverse momentum. For increasing transverse momenta the resolution decreases. It is better than  $100 \mu\text{m}$  for transverse momenta above  $1 \text{ GeV}/c$  [22] which gives the necessary spatial resolution for the determination of the position of the secondary vertex.

### 3.4 V0 detector

The V0 detector consists of 2 units of scintillating counters V0A and V0C which are respectively placed at  $z = -340 \text{ cm}$  and at  $z = 90 \text{ cm}$  from the interaction point [22]. The V0A covers a pseudorapidity range of  $2.8 < \eta < 5.1$  while the V0C covers the pseudorapidity range of  $-1.7 < \eta < -3.7$ . This detector setup is used as minimum bias trigger and demands coincident signals in both detectors with the crossing of both beams [23].

## 4 Track and event selection

### 4.1 Data

The data was collected in 2016, distributed over 31 runs, in which the main electron identification (eID) detectors were functioning well. In all samples combined a total of above  $297 \cdot 10^6$  events are available before application of any analysis cuts. After application of event cuts such as pile-up rejection and  $z$ -vertex cut  $252 \cdot 10^6$  events are still left for further analysis. Details on the event cuts can be derived from Chapter 4.4. The runs used for analysis are:

- 265309, 265332, 265334, 265336, 265338, 265339, 265342, 265343, 265344, 265377, 265377, 265378, 265381, 265383, 265384, 265385, 265387, 265388, 265419, 265420, 265421, 265422, 265424, 265426, 265427, 265435, 265499, 265500, 265501, 265521, 265525

### 4.2 Monte Carlo simulation

The Monte Carlo (MC) is a generated sample in which particles are “virtually” created and transported through the detector geometry and response. For particles from the MC sample exists the MC truth information in which all properties such as momentum, particle species, mother particle, et cetera are registered. The efficiency of the selection criteria is obtained by simultaneously applying the selection criteria on data and the MC. The efficiency of the selection criteria can be directly obtained by the MC truth information since the properties of the input and output are known. The MC sample was generated with the HIJING generator [43]. Since beauty- and charm-hadrons are rare the information about them have large statistical uncertainties [13]. Thus, the statistics of electrons from heavy-flavored hadron decays was enhanced by generating pp events with PYTHIA [44] where each event contains one  $\langle c\bar{c} \rangle$  and  $\langle b\bar{b} \rangle$  pair of which 500 % decay via electrons. Therefore they were added to the HIJING events. The MC sample consists of  $128 \cdot 10^6$  events in 31 runs. For comparability to data the detector status has to be similar to data in each run which is why the numbers of the runs in data and the MC are equal. The runs used for analysis are:

- 265309, 265332, 265334, 265336, 265338, 265339, 265342, 265343, 265344, 265377, 265377, 265378, 265381, 265383, 265384, 265385, 265387, 265388, 265419, 265420, 265421, 265422, 265424, 265426, 265427, 265435, 265499, 265500, 265501, 265521, 265525

### 4.3 Track selection

For analysis only tracks fulfilling various selection criteria, see Table 1, are taken into account. This corresponds to tracks which were reconstructed with the ITS and the TPC and originate from a single adequately reconstructed particle trajectory [25]. Kink particle rejection is one important aspect because these candidates are inconsistent with a track hypothesis of a continuous particle trajectory. These

direction changes arise from e.g. decays [26]. The reconstructed track must have “generated” a signal in 4 ITS layers and in atleast 110 out of 159 TPC pad rows (TPC clusters). Further details ca be found in [8].

Observable	Cut value
TPC and ITS refit	required
$\chi^2$ /TPC cluster	$< 4$
Kink mothers and daughters	rejected
Number of ITS clusters	$\geq 4$
Requirement of SPD pixels	both
Number of TPC clusters	$\geq 110$
Number of dE/dx clusters (PID clusters)	$\geq 80$
Ratio found/findable TPC clusters	$> 0.6$
DCA to the primary vertex in radial direction	$< 1$ cm
DCA to the primary vertex in $z$ -direction	$< 2$ cm

Table 1: Overview of standard track selection cuts.

The requirement of a DCA in  $xy$  plane to 1 cm and in  $z$  direction to 2 cm rejects only  $< 1\%$  of electrons from beauty-hadron decays [3]. Another requirement are hits in both SPD pixel layers to reduce the amount of electrons produced via photon conversion in the detector material at large distances from the primary vertex [3].

#### 4.4 Event selection

To only use good events all events for further analysis have to fulfill certain criteria [3]. Events with no SPD vertex or a primary vertex with less than one contributor to the vertex are removed [3]. Only events with a primary vertex within 10 cm from the nominal center of the coordinate system in direction of the beam are used ( $z < 10$  cm) [3]. Furthermore, the difference between both vertices in beam direction has to be below 0.5 cm and the resolution of the SPD vertex in  $z$ - direction has to be less than 0.25 cm [3]. All events are presented for minimum bias.

## 5 Electron identification

Target of this chapter is to describe how the electrons are extracted from the background of other charged particles. Various hadronic background sources occur but there are also muons that could be misidentified. Since the mass of muons and pions do not deviate much. The term pions will be used for both particle species in this chapter. In this chapter a selection on the impact parameter was applied, as described in Chapter 6, which reduces the hadron contamination additionally to the selection criteria described in Chapter 5.1 and Chapter 5.2. Thus, constant PID is possible up to  $p_T \leq 8 \text{ GeV}/c$  [49]. However, the impact parameter selection increases protons from secondary decays compared to no impact parameter cut. Only charged particles with  $p \geq 0.3 \text{ GeV}/c$  are detected by the TOF and TPC detectors due to strong magnetic field; nevertheless in the following the low momentum boundary will be pointed out multiple times as  $0 \text{ GeV}/c$  for better visualization. E.g. in the momentum interval of  $0 \leq p \leq 0.5 \text{ GeV}/c$  charged particles only exist in the momentum interval of  $0.3 \leq p \leq 0.5 \text{ GeV}/c$ .

### 5.1 Electron identification with the TOF detector

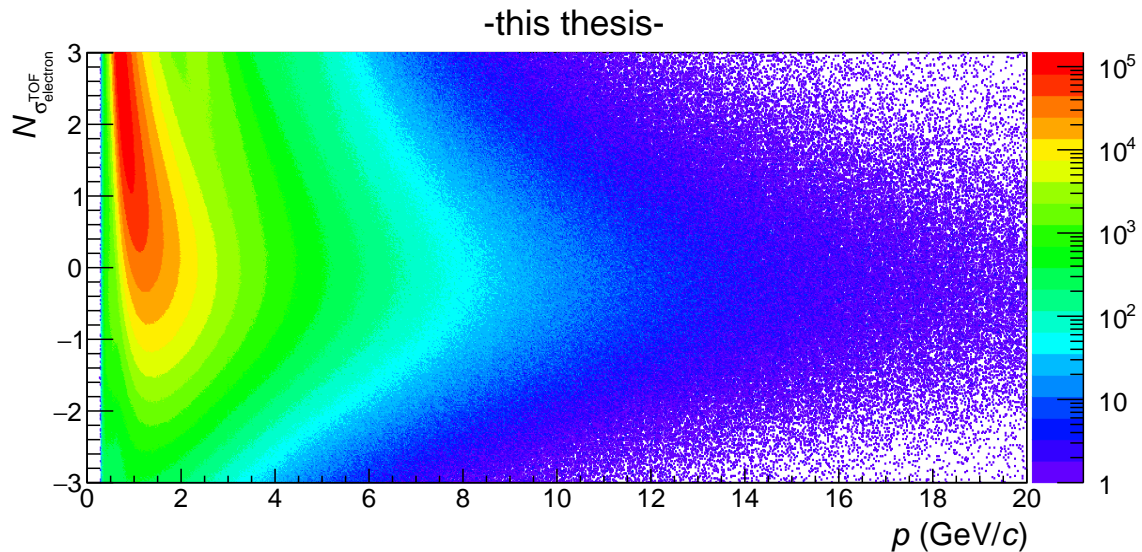
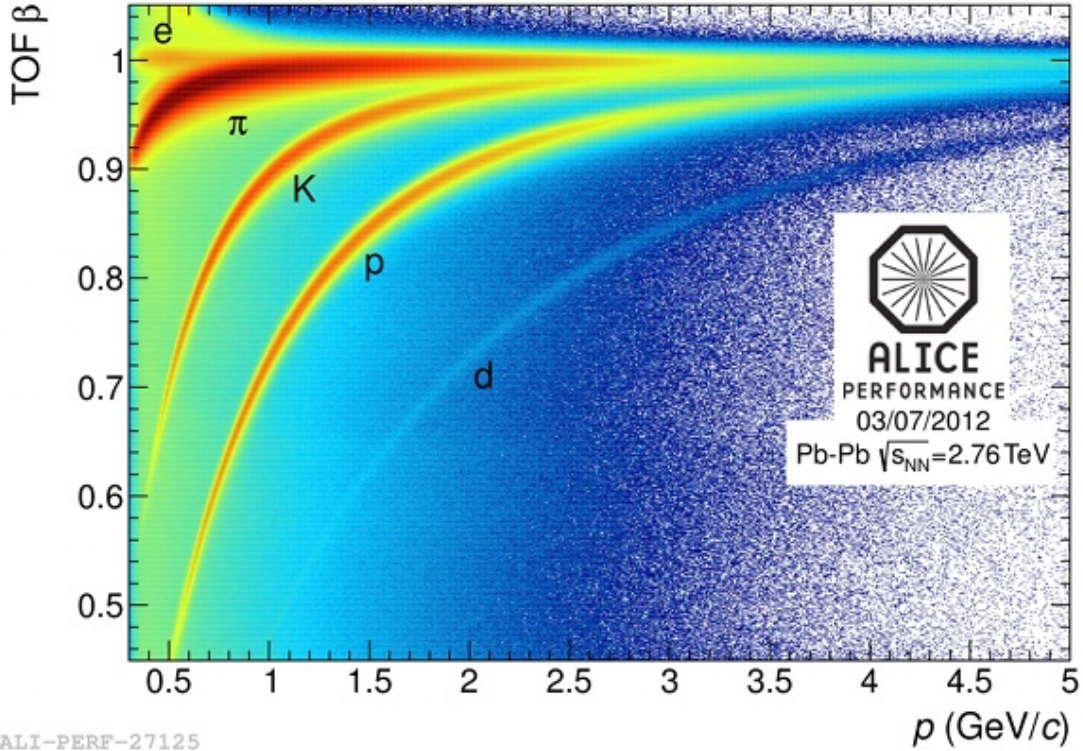


Figure 9:  $N_{\sigma_{\text{electron}}^{\text{TOF}}}$  as a function of momentum in p–Pb collisions at  $\sqrt{s_{\text{NN}}} = 5.02 \text{ TeV}$ .

For electron identification (eID) with the TOF detector the property  $N_{\sigma_{\text{electron}}^{\text{TOF}}}$ , explained in Chapter 3.1, is used. In Fig. 9 the  $N_{\sigma_{\text{electron}}^{\text{TOF}}}$  distribution is plotted in dependence of momentum after a cut of  $|N_{\sigma_{\text{electron}}^{\text{TOF}}}| \leq 3\sigma$ . The  $N_{\sigma_{\text{electron}}^{\text{TOF}}}$  distribution is centered around 0 with a standard deviation of approximately 1. The distribution of  $N_{\sigma_{\text{electron}}^{\text{TOF}}}$  matches a Gaussian distribution due to the fact that the measured velocity of high ultra relativistic electrons is randomly distributed around  $\beta \approx 1$  caused by the finite detector resolution. Assuming highly relativistic electrons is justified since the minimum momentum detected by the TOF detector is  $0.3 \text{ GeV}/c$ .



ALI-PERF-27125

Figure 10: Velocity  $\beta$  versus momentum with bands for different particle species [21].

GeV/ $c$ . The variable  $N_{\sigma_{\text{electron}}^{\text{TOF}}}$  is defined as the difference between time measured and time expected for electrons divided by the detector resolution. Particles which are slower than the hypothesis for electrons have positive values of  $N_{\sigma_{\text{electron}}^{\text{TOF}}}$ . The heavier hadrons are slower for the same momentum and disturb the symmetry of the Gaussian distribution in the positive area of the  $N_{\sigma_{\text{electron}}^{\text{TOF}}}$  distribution in Fig. 9 leading to an asymmetric shape of the distribution. Origin of the asymmetry of entries for momenta  $p < 1$  GeV/ $c$  are pions due to their small mass of  $139 \text{ MeV}/c^2$  which can be seen in Fig. 10 where electrons and pions can not be separated by velocity for momenta above approximately  $0.5$  GeV/ $c$ . In Fig. 10 the velocity  $\beta$  measured with the TOF detector versus momentum is shown. Distinct bands occur for the different particle species which vanish for increasing momentum. The heavier a particle species is, the later its band merges with the other bands. For momenta up to  $1.5$  GeV/ $c$  for kaons and up to  $3$  GeV/ $c$  for protons a distinction from electrons is still possible by using only the TOF detector. In this thesis eID with the TOF detector is used within the full range in momentum since a negligible amount of approximately  $0.3\%$  of all electrons are rejected by the  $|N_{\sigma_{\text{electron}}^{\text{TOF}}}| \leq 3\sigma$  cut [49].

For further analysis Fig. 9 was investigated in more detail. By a projection of the  $N_{\sigma_{\text{electron}}^{\text{TOF}}}$  distribution in momentum slices the different momentum intervals were analyzed. Due to the decreasing amount of entries for increasing momentum the range in momentum for the described projection varied depending on the momentum

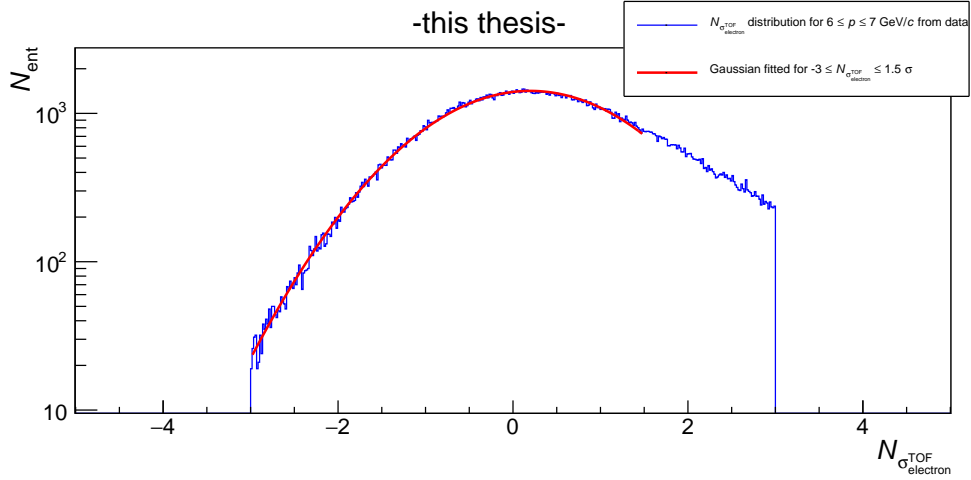


Figure 11:  $N_{\sigma_{\text{electron}}^{\text{TOF}}}$  distribution for  $6 \leq p \leq 7$  GeV/ $c$  in p–Pb collisions at  $\sqrt{s_{\text{NN}}} = 5.02$  TeV.

interval. In the momentum interval of  $0 \leq p \leq 1.5$  GeV/ $c$  a Gaussian fit could not be used because electron band, pion band and kaon band merge in this momentum interval. The spectrum of  $1.5 \leq p \leq 20$  GeV/ $c$  was divided into three areas,  $1.5 \leq p \leq 4$ ,  $4 < p \leq 10$  and  $10 < p \leq 20$  GeV/ $c$ . For the low  $p$  interval each momentum slice had a width of 0.5 GeV/ $c$  while it was 1 GeV/ $c$  in the second and 2.5 GeV/ $c$  in the third interval. An example projection for the momentum interval of  $6 \leq p \leq 7$  GeV/ $c$  is shown in Fig. 11. Due to the “approaching” hadron distribution for lower momenta and the cut right tail the Gaussian fit (in red) covers the range between  $-3 \leq N_{\sigma_{\text{electron}}^{\text{TOF}}} \leq 1.5\sigma$ . With a  $\chi_{\text{red}}^2 = 1.23$  fit and data differ only slightly.

The fit results of the MC and data are compared in Fig. 12. Shown are mean and standard deviation of the Gaussian fit on the  $y$ -axis in dependence of momentum. The corresponding fit results do not match within uncertainties of the fit. In addition the difference between the standard deviations of the Gaussian fits from data and MC divided by the standard deviation from MC is shown in the upper panel of Fig. 13. The difference of the means in is shown in the lower panel of Fig. 13. The deviations between the standard deviations is below 9 % and below  $0.32 N_{\sigma_{\text{electron}}^{\text{TOF}}}$  for the means. The main purpose of the TOF detector is to reduce contamination caused by kaons up to 1.5 GeV/ $c$  and up to 3 GeV/ $c$  for protons [49] which is used to improve the measurement with the TPC significantly. This is achieved by the selection of  $\left| N_{\sigma_{\text{electron}}^{\text{TOF}}} \right| \leq 3\sigma$  [49] [3].

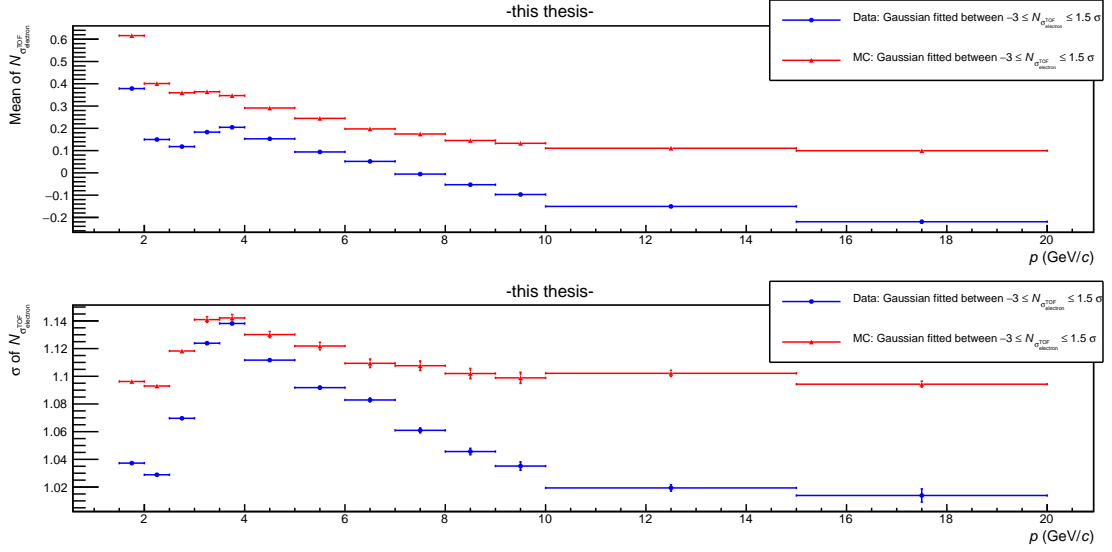


Figure 12: Comparison of the Gaussian fit parameters of the  $N_{\sigma_{\text{electron}}^{\text{TOF}}}$  distribution from MC and data in p–Pb collisions at  $\sqrt{s_{\text{NN}}} = 5.02$  TeV.

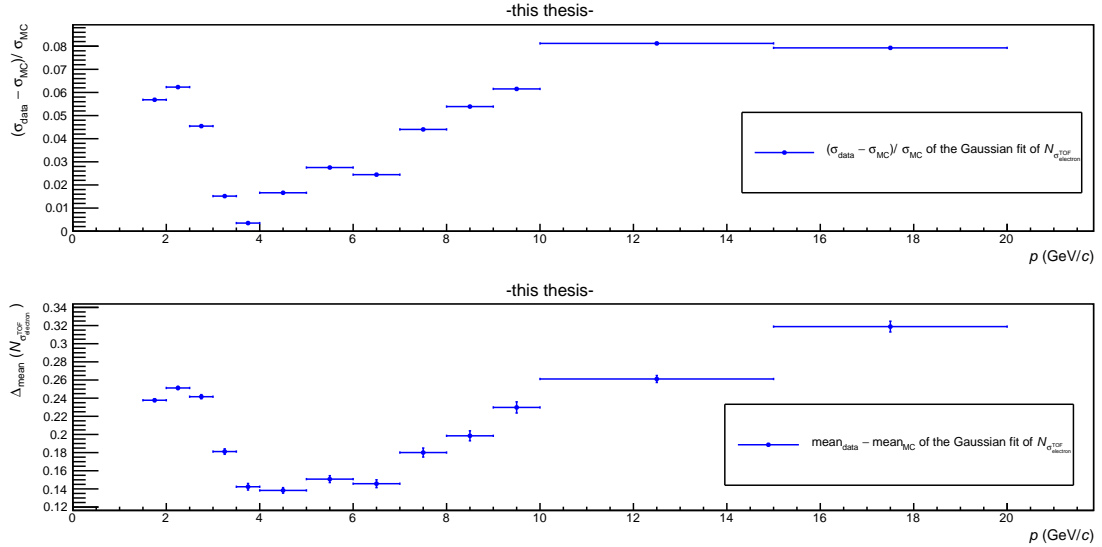


Figure 13: Difference between the standard deviations of the Gaussian fits from data and MC divided by the standard deviation from MC and difference between the means of the Gaussian fits of the  $N_{\sigma_{\text{electron}}^{\text{TOF}}}$  distribution from MC and data in p–Pb collisions at  $\sqrt{s_{\text{NN}}} = 5.02$  TeV.

## 5.2 Electron identification with the TPC detector

The specific energy loss measured with the TPC is used to distinguish electrons from other charged particles. In theory the TPC is calibrated in a way that the  $N_{\sigma_{\text{electron}}^{\text{TPC}}}$  distribution is pseudorapidity independent. In addition, all runs used for analysis should be consistent. These two properties are therefore analyzed in order to remove possible incongruities.

## 5.2.1 Momentum dependence

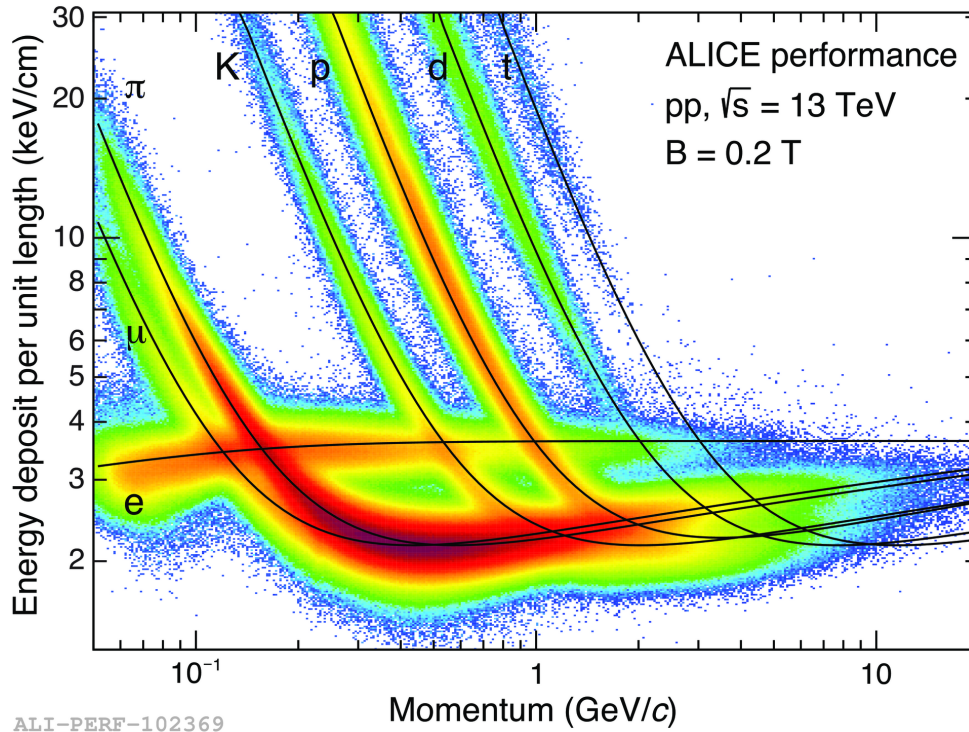


Figure 14: Energy loss vs momentum for charged particles of various species [51].

In Fig. 14 the energy loss of various charged particles is plotted versus momentum. Discrete lines indicate the expected energy loss for the respective particle species. The electron line differs from the shape of the line of the other particle species because for momenta of the order of  $\text{GeV}/c$  the energy loss of the electrons is constant which corresponds to the “Fermi Plateau” of the Bethe-Bloch formula [41]. This is not yet the case for  $\pi$ ,  $K$ ,  $p$  and  $d$  at low momenta due to their bigger masses. Therefore the energy loss distribution of electrons is intersected by all other particle species. The intersection differs mostly in momentum since the energy loss is nearly constant for the “Fermi Plateau” and the hadrons have not reached the “Fermi Plateau” yet.

In this case the energy loss determined by the TPC detector does not contain enough information for separating hadrons and electrons. Therefore the information provided by the TOF detector also has to be taken into account for PID. Figure 15 shows the  $N_{\sigma_{\text{electron}}^{\text{TPC}}}$  distribution defined in Eq. 6, versus momentum after a cut on  $|N_{\sigma_{\text{electron}}^{\text{TOF}}}| \leq 3\sigma$  has been applied. The electrons can be found in a range of  $|N_{\sigma_{\text{electron}}^{\text{TPC}}}| \leq 3\sigma$  around 0  $N_{\sigma_{\text{electron}}^{\text{TPC}}}$  while a large hadron distribution, mainly pions, is in a negative area of  $N_{\sigma_{\text{electron}}^{\text{TPC}}}$ . Furthermore, the intersections of the energy loss distribution of electrons with other particle species can also be seen in Fig. 15 in form of lines crossing the electron distribution. A comparison with Fig. 14 shows that the first line is caused by kaons while the second line is caused by protons. These lines occur even though the  $N_{\sigma_{\text{electron}}^{\text{TOF}}}$  selection has been applied. By a comparison of

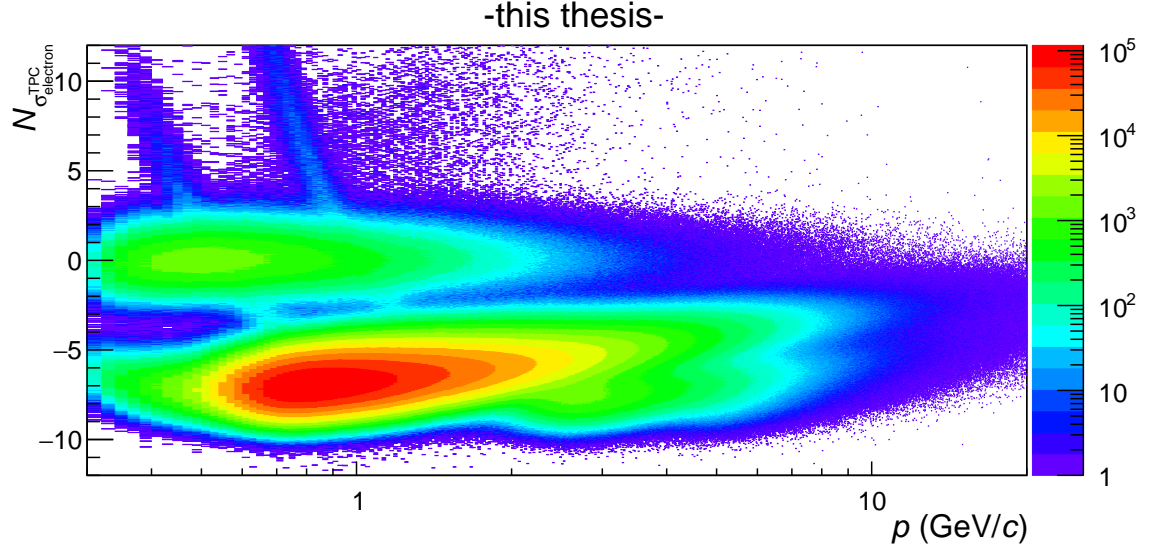


Figure 15:  $N_{\sigma_{\text{electron}}^{\text{TPC}}}$  distribution after  $N_{\sigma_{\text{electron}}^{\text{TOF}}}$  cut as a function of momentum in p–Pb collisions at  $\sqrt{s_{\text{NN}}} = 5.02$  TeV.

the amount of entries of kaon and proton line in Fig. 14 and in Fig. 15 it becomes evident that the contamination has already been reduced significantly.

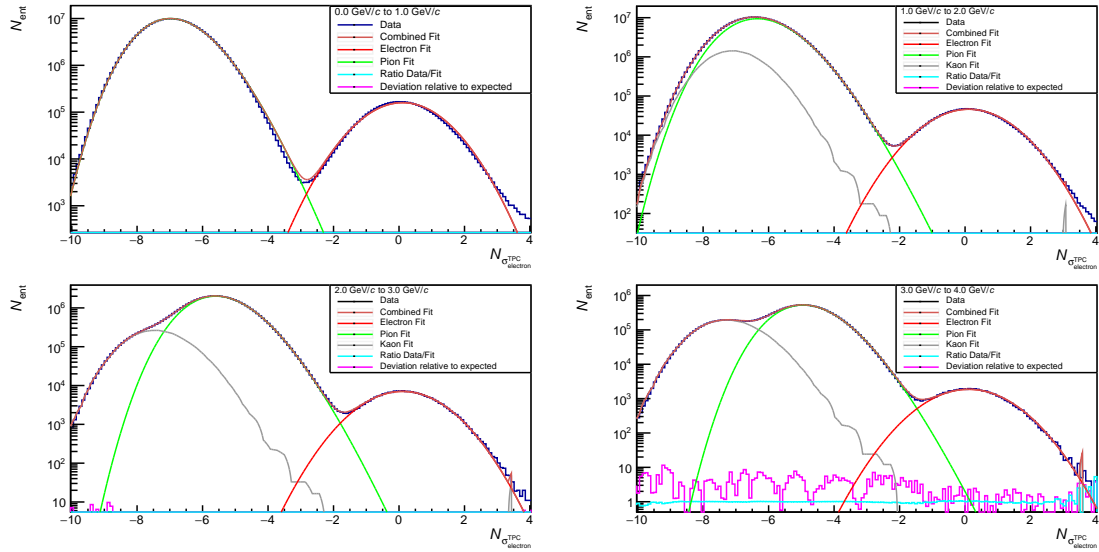


Figure 16: Projection of the  $N_{\sigma_{\text{electron}}^{\text{TPC}}}$  distribution after TOF cut fitted by various fit functions in p–Pb collisions at  $\sqrt{s_{\text{NN}}} = 5.02$  TeV.

Analog to the method described in Chapter 5.1, as shown in Fig. 11 the same procedure was used for the  $N_{\sigma_{\text{electron}}^{\text{TPC}}}$  distribution after application of the  $N_{\sigma_{\text{electron}}^{\text{TOF}}}$  selection. Since for high momenta only fewer electrons exist and the electron distribution becomes overlapped by the hadron distribution the range in momentum was  $0 \leq p \leq 6$  GeV/c with a momentum width of 0.5 GeV/c for momenta below 4 GeV/c and 1 GeV/c for higher momenta. The pion  $dE/dx$  distribution is the dominant background source and situated at negative values for  $N_{\sigma_{\text{electron}}^{\text{TPC}}}$  in this momen-

tum range. Therefore, a Gaussian fit was used in a range of  $-1 \leq N_{\sigma_{\text{electron}}^{\text{TPC}}} \leq 3\sigma$ . The left boundary was obtained by usage of various fits for the various particle species. An example is shown in Fig. 16 where the distributions of pions and kaons overlap the electron distribution. Here, e.g. the pion distribution is well described by a Landau multiplied with an exponential tail. The number of entries is plotted versus  $N_{\sigma_{\text{electron}}^{\text{TPC}}}$  for various momentum intervals showing how the overlap or contamination depends on momentum. The amount of entries decreases for increasing momentum. In order to limit the contamination as much as possible while ensuring a precise determination of the fit parameters (in order to reduce the systematic uncertainty as much as possible) the left boundary was determined as  $-1 N_{\sigma_{\text{electron}}^{\text{TPC}}}$ .

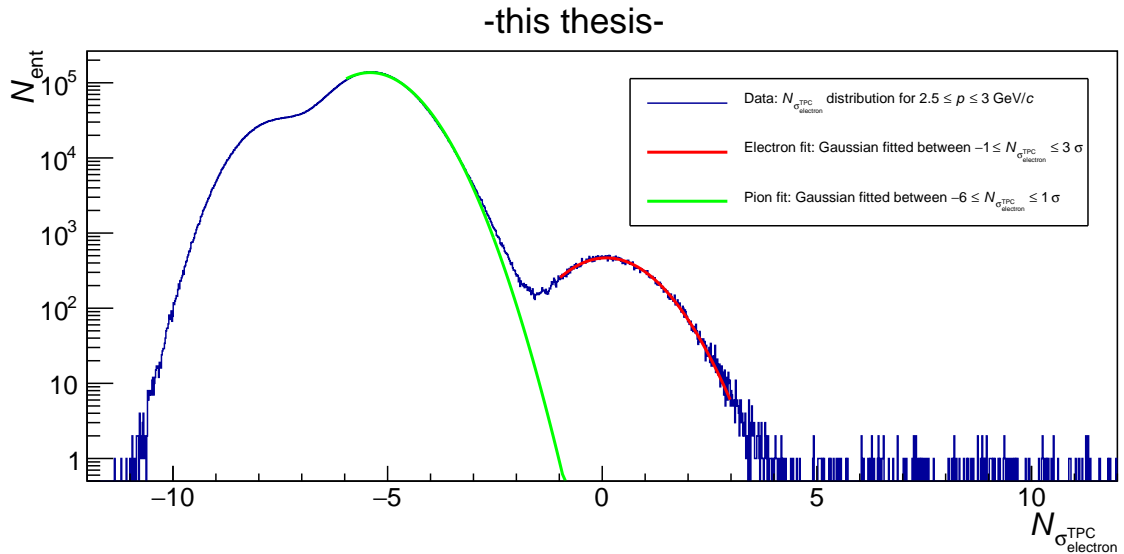


Figure 17: Projection of the  $N_{\sigma_{\text{electron}}^{\text{TPC}}}$  distribution after TOF cut for  $2.5 \leq p \leq 3.0$  GeV/c in p–Pb collisions at  $\sqrt{s_{\text{NN}}} = 5.02$  TeV.

In Fig. 17 an example of the  $N_{\sigma_{\text{electron}}^{\text{TPC}}}$  distribution for a momentum range of  $2.5 \leq p \leq 3$  GeV/c is shown. Most entries come from the hadrons, mainly pions fitted by a Gaussian in green between  $-6 \leq N_{\sigma_{\text{electron}}^{\text{TPC}}} \leq 1\sigma$  ( $\chi_{\text{red}}^2 = 165$ ), covering the interval of  $-12 \leq N_{\sigma_{\text{electron}}^{\text{TPC}}} \leq -0.5\sigma$  which is followed by the electron candidates in a range of  $-3 \leq N_{\sigma_{\text{electron}}^{\text{TPC}}} \leq 3\sigma$  ( $\chi_{\text{red}}^2 = 1.07$ ). In Fig. 18 the fit results from MC and data are shown which do not agree within fit uncertainties. In addition, the difference of the standard deviations of the Gaussian fits from data and MC divided by the standard deviation from MC is shown in the upper panel of Fig. 19 while the lower panel shows the deviations between the means. For momenta above 5 GeV/c mean and standard deviation from data deviate stronger from the corresponding average value (about  $0.29 \sigma_{\text{electron}}^{\text{TPC}}$  for the means and about  $0.14 \sigma_{\text{electron}}^{\text{TPC}}$  for the standard deviations) since the amount of entries of electron candidates decreases which causes a worse fit. This is not the case for MC since the electrons are enhanced in MC. For momenta below 5 GeV/c the standard deviations from data and MC deviate less than 5% while the means deviate less than  $0.15 N_{\sigma_{\text{electron}}^{\text{TPC}}}$ . By calculating the fraction of electrons with a Gaussian approach in the range of  $-1$  to  $3$  times the standard deviation around the mean the amount of electrons does only vary below

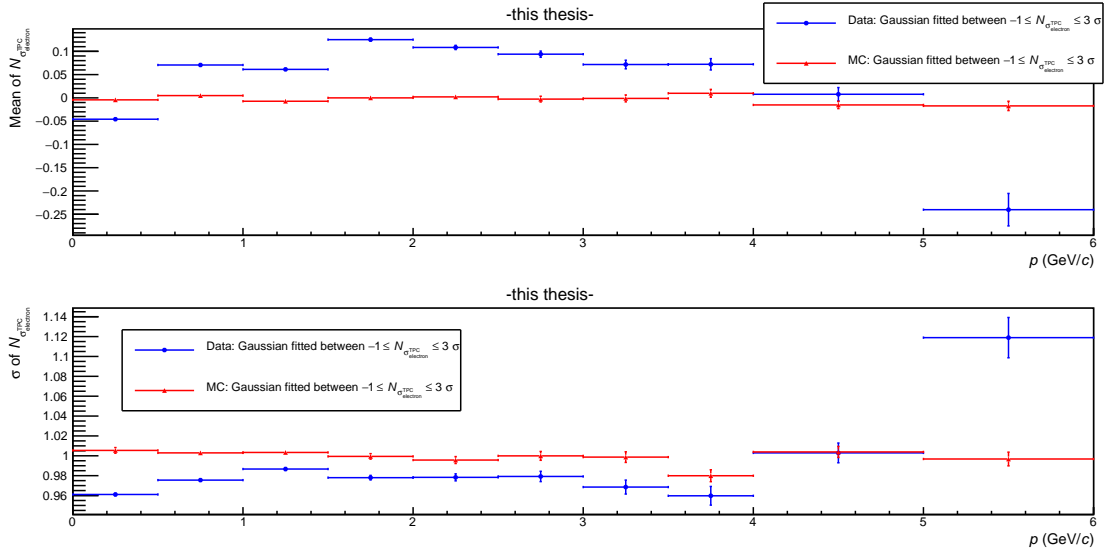


Figure 18: Comparison of the Gaussian fit parameters of the  $N_{\sigma_{\text{electron}}^{\text{TPC}}}$  distribution from MC and data in p–Pb collisions at  $\sqrt{s_{\text{NN}}} = 5.02$  TeV.

2.5 % between data and MC. Thus, the deviations between data and the MC are small for calculating the electron yield.

Furthermore the hadron contamination as a fraction of the electron sample obtained for the fits of the various particle species is shown in Fig 20 in the momentum range of  $1.4 \leq p \leq 8.4$  GeV/ $c$ . The contamination increases with increasing momentum since the overlap of the electron distribution with the distribution of pions increases. For a selection of  $-0.5 \leq N_{\sigma_{\text{electron}}^{\text{TPC}}} \leq 3\sigma$  the contamination is at maximum 15,4 % and below 3 % for momenta below 6 GeV/ $c$  while a high efficiency of about 69 % is fulfilled [49]. Thus, this selection was used to determine the inclusive electron yield.

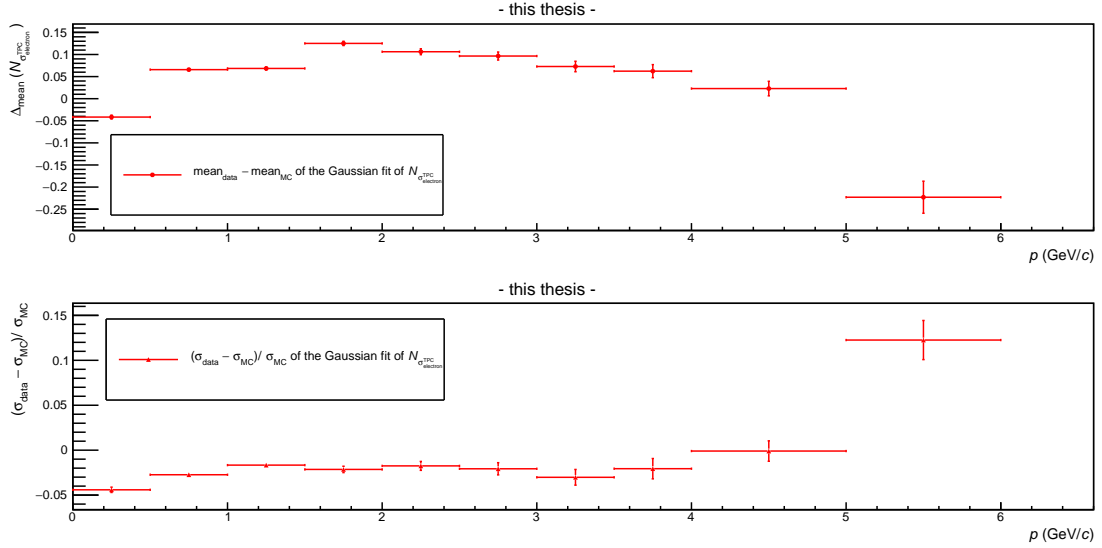


Figure 19: Ratio of the standard deviations and difference between the means of the Gaussian fits of the  $N_{\sigma_{\text{TPC}}}$  distribution from MC and data in p–Pb collisions at  $\sqrt{s_{\text{NN}}} = 5.02$  TeV.

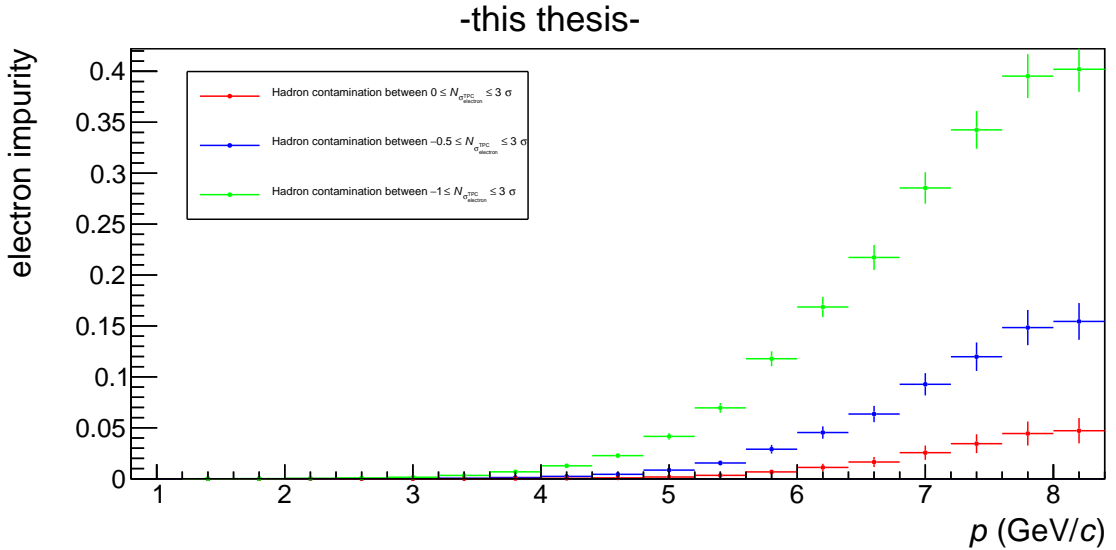


Figure 20: Hadron contamination in dependence of momentum for various  $N_{\sigma_{\text{TPC}}}$  cuts in p–Pb collisions at  $\sqrt{s_{\text{NN}}} = 5.02$  TeV.

### 5.2.2 Pseudorapidity dependence

To describe a particle's trajectory relative to the beam axis the spatial coordinate pseudorapidity ( $\eta$ ) is often used which is defined as:

$$\eta \equiv -\ln \left[ \tan \left( \frac{\theta}{2} \right) \right] = \frac{1}{2} \ln \left( \frac{|\mathbf{p}| + p_L}{|\mathbf{p}| - p_L} \right) \quad (7)$$

The variables defined in this equation are  $p :=$  momentum,  $p_L :=$  momentum along the beam axis and  $\theta :=$  polar angle. With the detector setup data was recorded in a pseudorapidity range of  $|\eta| \leq 0.8$  to provide long tracks in the TPC. For different polar angles the projection of the track on the pad plane and therefore the measured signal and specific ionization energy loss varies. In order to remove this angular dependence, the TPC has to be well calibrated thus the measured specific ionization energy loss depends only on momentum. Unfortunately this was not completely the case for the data used in this thesis. In dependence of  $\eta$  the  $N_{\sigma_{\text{electron}}^{\text{TPC}}}$  distribution was analyzed. In addition, the range in momentum of  $0 \leq p \leq 5$  GeV/ $c$  was used since in this momentum interval the hadron contamination is at maximum 5 %. The pseudorapidity dependence was analyzed in the range of  $-0.8 \leq \eta \leq 0.8$  in steps of 0.1 pseudorapidity units analog to Chapter 5.2.1 where the momentum dependence was obtained. The projections from data and MC were fitted with a Gaussian in the range of  $-1\sigma \leq N_{\sigma_{\text{electron}}^{\text{TPC}}} \leq 3\sigma$ . The fit results are shown in Fig. 21 where the pseudorapidity is plotted on the  $x$ -axis while mean and standard deviation are on the  $y$ -axis. In the upper panel of Fig. 21 the mean of the electron distribution from data and MC is shown where the green line represents a logistic growth fit of the mean from data which deviates from the approximately constant mean from MC (fluctuations below 2 %). The logistic growth fit is not symmetric around 0 pseudorapidity but shifted by about  $-0.065$  pseudorapidity units. Its equation is given in Chapter 9 in Eq 9. Due to the logistic growth the specific energy loss measured with the TPC is not pseudorapidity independent and has to be corrected. One possible explanation is the asymmetry of the collision setup of p–Pb. In addition, the lower panel of Fig. 21 shows the standard deviations of the electron distributions from data and MC which differ by about 4 % with overall changes of about 1 % over the full pseudorapidity range.

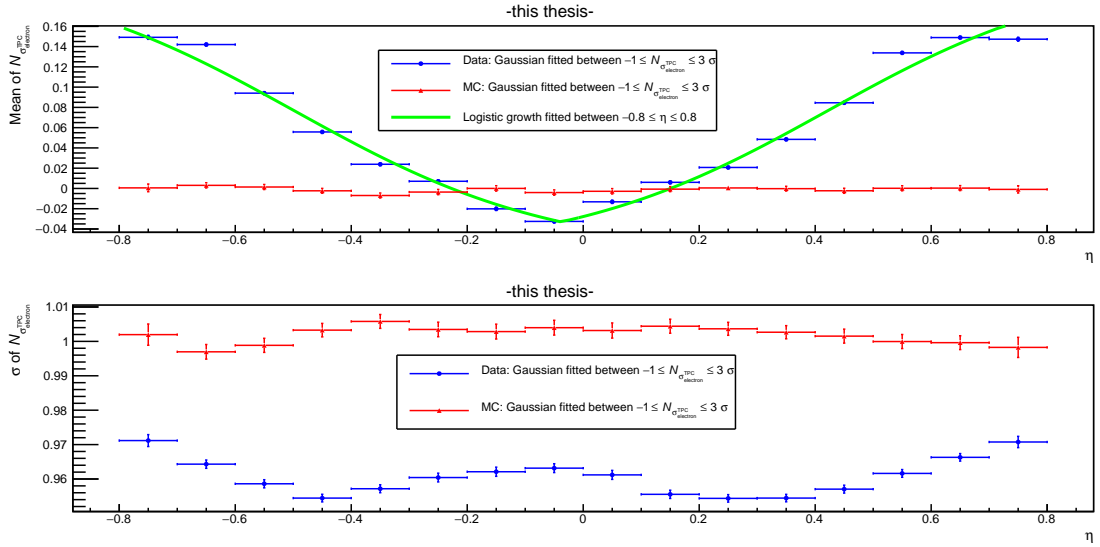


Figure 21: Fit parameters of pseudorapidity slices from data and MC in comparison in p–Pb collisions at  $\sqrt{s_{\text{NN}}} = 5.02$  TeV.

### 5.2.3 Electrons per event

A run wise consideration of the electrons per event ensures that all runs taken into account for analysis are consistent since the amount particles of a certain particle species should be constant per event and independent of the run index. Thus, also the amount of electrons per event should be constant. Furthermore a comparison of data and MC is possible. If the small fluctuations of the electrons per event in dependence of the run index is well represented by the MC the ratio  $(\frac{N_{\text{electrons}}}{N_{\text{events}}})_{\text{data}} / (\frac{N_{\text{electrons}}}{N_{\text{events}}})_{\text{MC}}$  is constant. To do so, different momentum intervals were inspected. Mean and standard deviation were obtained run wise by the projection method of Chapter 5.2.1. Therefore, the corresponding fit parameters were used to calculate the amount of electrons  $N_{\text{electrons}}$  in each run by calculating the integral of the distribution scaled by bin and momentum width. This value was divided by the number of events  $N_{\text{events}}$  in each run. The value of  $\frac{N_{\text{electrons}}}{N_{\text{events}}}$  is slightly depending on the run index. This is well reproduced in MC which can be seen in Fig. 22 where  $(\frac{N_{\text{electrons}}}{N_{\text{events}}})_{\text{data}} / (\frac{N_{\text{electrons}}}{N_{\text{events}}})_{\text{MC}}$  is shown in dependency of the run index. The zero degree polynomial describes the points well ( $\chi_{\text{red}}^2 = 1.93$ ).

Thus, in this momentum range  $(\frac{N_{\text{electrons}}}{N_{\text{events}}})_{\text{data}} / (\frac{N_{\text{electrons}}}{N_{\text{events}}})_{\text{MC}}$  is independent of the run index concluding that the data is well represented by the MC. For higher momenta  $(\frac{N_{\text{electrons}}}{N_{\text{events}}})_{\text{data}} / (\frac{N_{\text{electrons}}}{N_{\text{events}}})_{\text{MC}}$  spreads more due to the decrease of entries for increasing momentum and therefore sensitivity towards statistical fluctuations. Thus, this leads also to larger fluctuations of  $\frac{N_{\text{electrons}}}{N_{\text{events}}}$  which can be seen in the appendix in Fig. 34.

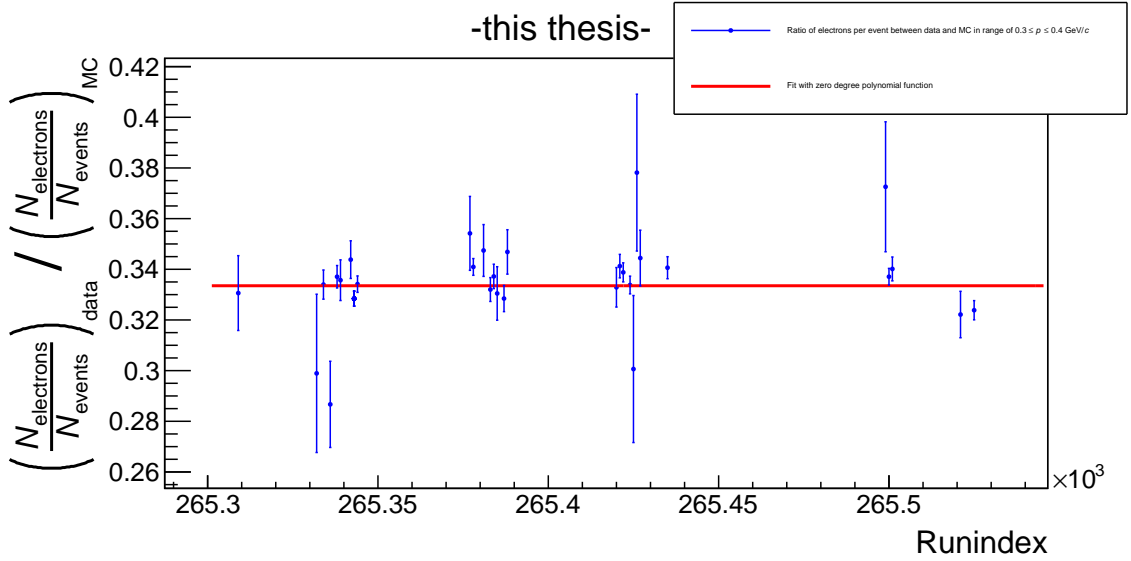


Figure 22:  $(\frac{N_{\text{electrons}}}{N_{\text{events}}})_{\text{data}} / (\frac{N_{\text{electrons}}}{N_{\text{events}}})_{\text{MC}}$  for  $0.3 \leq p \leq 0.4$  GeV/c in p–Pb collisions at  $\sqrt{s_{\text{NN}}} = 5.02$  TeV.

### 5.3 Summary for eID

It was shown in [49] that a selection of  $|N_{\sigma_{\text{electron}}^{\text{TOF}}}| \leq 3\sigma$  and a range of  $-0.5 \leq N_{\sigma_{\text{electron}}^{\text{TPC}}} \leq 3\sigma$  ensure a precise separation of electrons from other charged particles. This selection has an efficiency about 69% [49]. The cut of  $N_{\sigma_{\text{electron}}^{\text{TOF}}}$  reduces significantly hadron contamination caused by kaons for momenta below 1.5 GeV/c and for momenta below 3 GeV/c for protons. A selection of  $-0.5 \leq N_{\sigma_{\text{electron}}^{\text{TPC}}} \leq 3\sigma$  suppresses the contamination caused by pions and other hadrons sharply. Furthermore the impact parameter cut additionally decreases the hadron contamination and the resulting electron impurity is shown in Fig. 20. Finally electrons are identified and separated.

## 6 Impact parameter distribution

As described in Chapter 2 the signal-to-background ratio for electrons originating from beauty-hadron decays is increased by a cut on the impact parameter. This also reduces the hadron contamination. The impact parameter distribution in  $xy$ -plane and in  $z$ -direction were analyzed. Since target of this thesis is the raw electron yield in dependence of  $p_T$  only the analysis results of the  $xy$ -plane are shown here. Results for the impact parameter in  $z$ -direction are shown in the appendix in Chapter 9.

### 6.1 Momentum dependence

In Fig. 23 the  $d_{xy}$  distribution is shown in dependence of  $p_T$ . The number of entries decreases with increasing impact parameter and the center of the distribution is centered at approximately  $0 \mu\text{m}$ . In addition, the amount of entries decreases with increasing  $p_T$  and also the width of the  $d_{xy}$  distribution narrows.

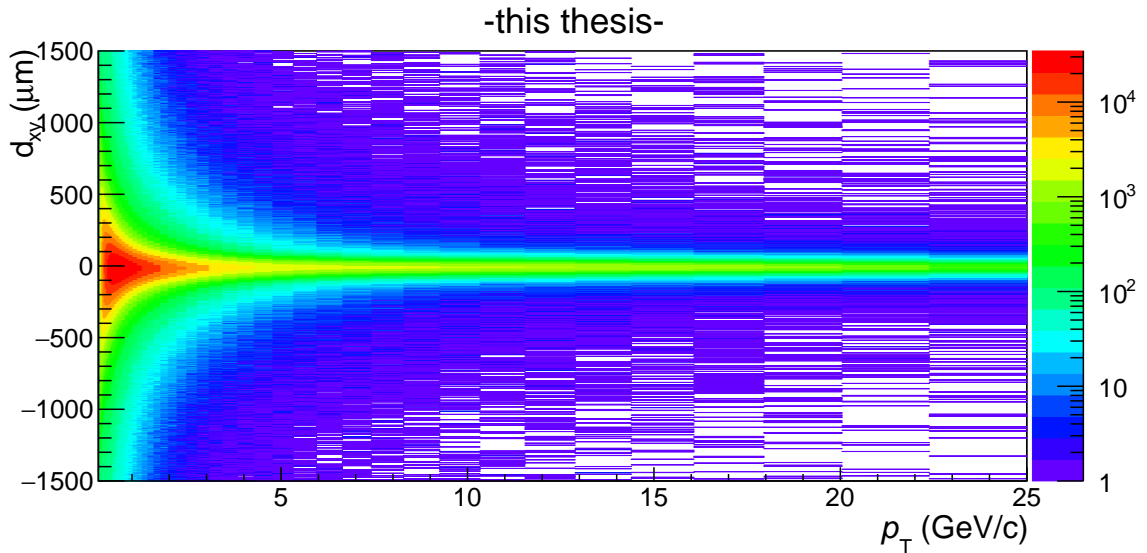
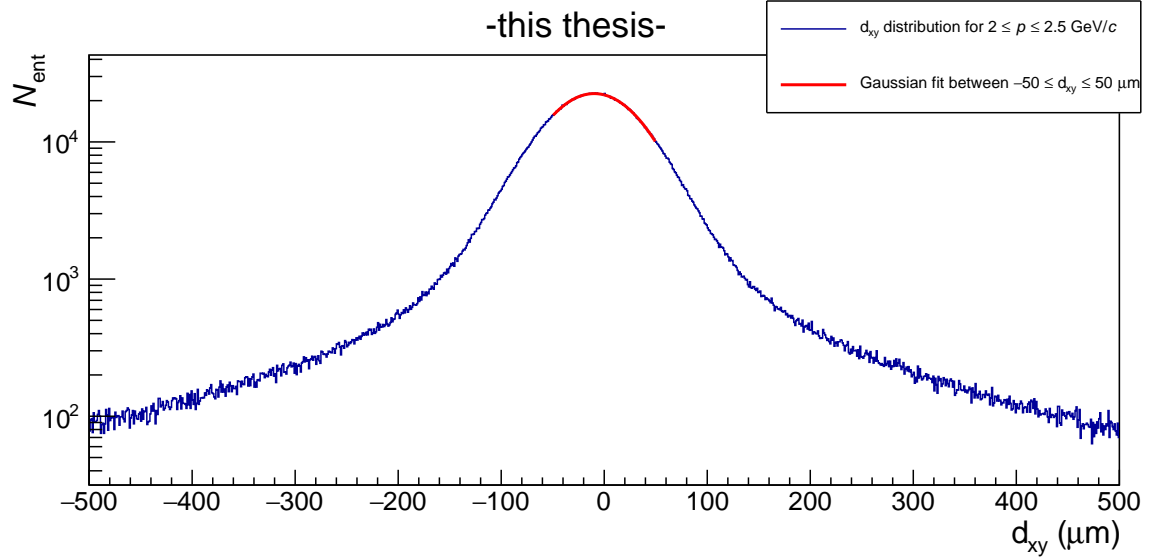


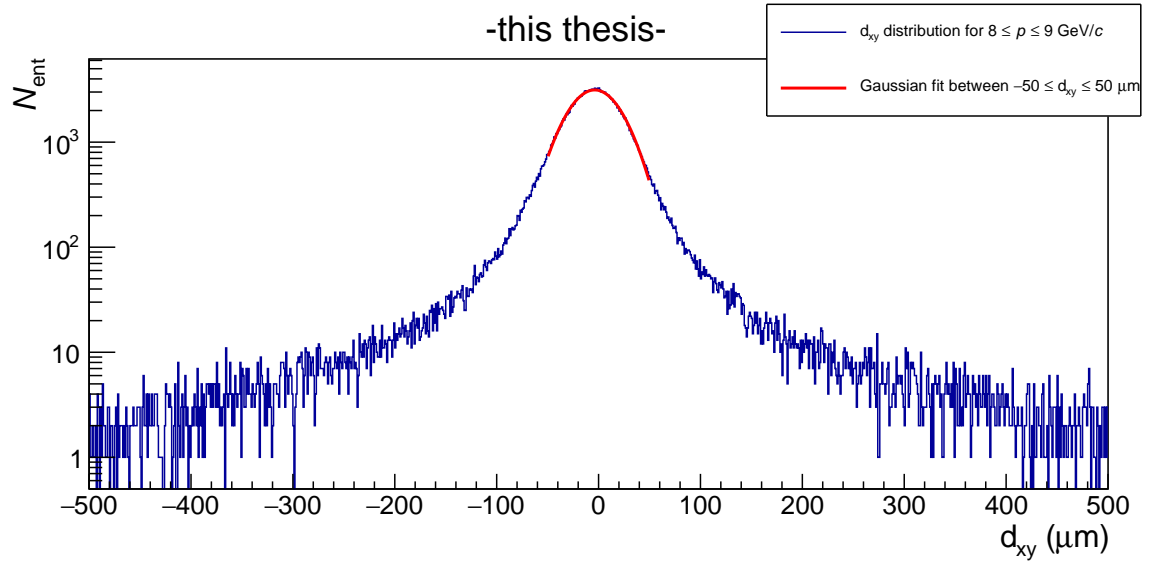
Figure 23:  $d_{xy}$  distribution in dependence of  $p_T$  in p-Pb collisions at  $\sqrt{s_{NN}} = 5.02$  TeV.

This distribution was inspected in momentum slices with an analog procedure as in Chapter 5.2.1. The whole spectrum of  $25 \text{ GeV}/c$  was divided into the regions  $0 \leq p_T \leq 4$ ,  $4 < p_T \leq 10$  and  $10 < p_T \leq 25 \text{ GeV}/c$  with a width of  $0.5$ ,  $1.0$  and  $2.5 \text{ GeV}/c$  for each momentum slice in the respective region. A Gaussian fit function was used in a small impact parameter range of  $-50 \leq d_{xy} \leq 50 \mu\text{m}$  because the width of the  $d_{xy}$  distribution is depending on  $p_T$ .

Two momentum slices are shown in a range of  $-500 \leq d_{xy} \leq 500 \mu\text{m}$  in Fig. 24. The data is well described by the fit in Fig. 24a ( $\chi_{red}^2 = 1.18$ ) and also in Fig. 24b ( $\chi_{red}^2 = 1.66$ ). The amount of entries between  $-1500 \leq d_{xy} \leq 1500 \mu\text{m}$  decreases from about  $3 \cdot 10^6$  for  $2 < p_T \leq 2.5 \text{ GeV}/c$  to  $2.2 \cdot 10^4$  for  $8 < p_T \leq 9 \text{ GeV}/c$ .



(a)  $d_{xy}$  distribution for the momentum interval  $2 \leq p_T \leq 2.5 \text{ GeV}/c$ .



(b)  $d_{xy}$  distribution for the momentum interval  $8 \leq p_T \leq 9 \text{ GeV}/c$ .

Figure 24:  $d_{xy}$  distribution for various momentum intervals in p–Pb collisions at  $\sqrt{s_{NN}} = 5.02 \text{ TeV}$ .

In addition, the MC was also inspected in momentum slices and the obtained fit parameters were compared with the corresponding values for data as shown in Fig. 25 and Fig. 26. For increasing  $p_T$  the mean increases while the standard deviation decreases. The mean for data is shifted from about  $-15 \mu\text{m}$  for  $0 \leq p_T \leq 1 \text{ GeV}/c$  towards about  $-6 \mu\text{m}$  for  $20 \leq p_T \leq 25 \text{ GeV}/c$  concluding that the mean for data is shifted about  $9 \mu\text{m}$  over the full range in  $p_T$ . For MC the shift from about  $-14 \mu\text{m}$  for  $0 \leq p_T \leq 1 \text{ GeV}/c$  towards  $-3 \mu\text{m}$  for  $20 \leq p_T \leq 25 \text{ GeV}/c$  amounts about  $11 \mu\text{m}$ . The standard deviation obtained for data decreases from  $154 \mu\text{m}$  for  $0 \leq p_T \leq 1 \text{ GeV}/c$  towards  $21 \mu\text{m}$  for  $20 \leq p_T \leq 25 \text{ GeV}/c$ . Thus, an overall shift of about  $133 \mu\text{m}$  occurs. For MC the standard deviation is shifted about  $121 \mu\text{m}$  from about  $144 \mu\text{m}$  for  $0 \leq p_T \leq 1 \text{ GeV}/c$  towards  $23 \mu\text{m}$  for  $20 \leq p_T \leq 25 \text{ GeV}/c$ .

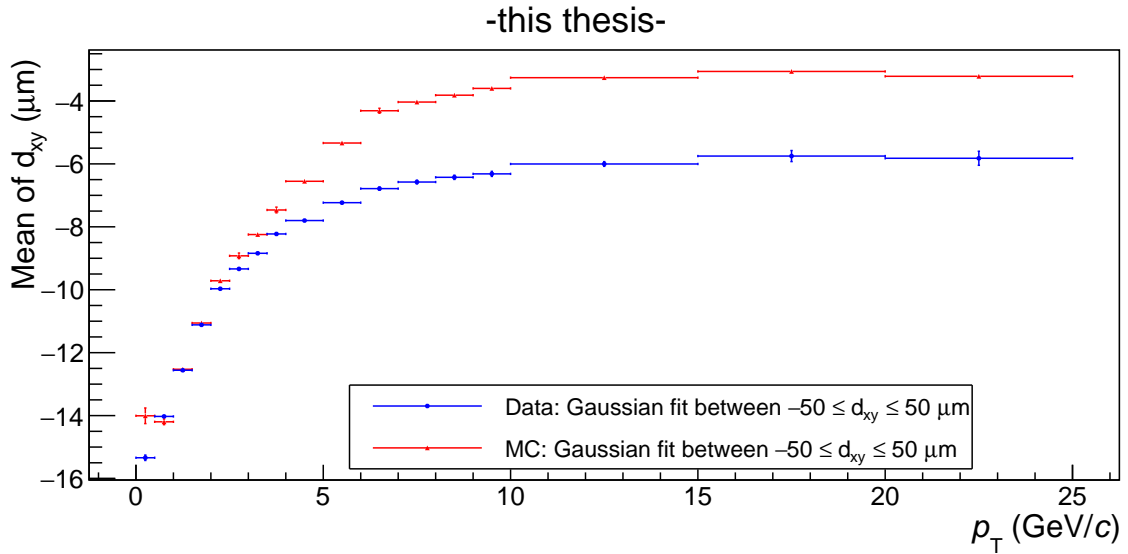


Figure 25: Comparison of the Gaussian mean of the  $d_{xy}$  projection for data and MC in p–Pb collisions at  $\sqrt{s_{NN}} = 5.02 \text{ TeV}$ .

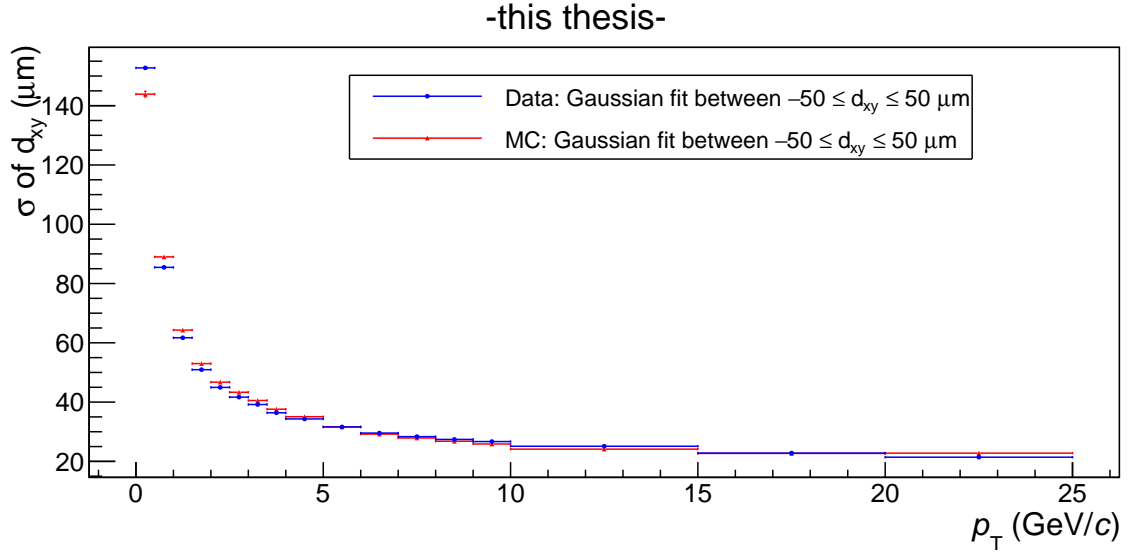
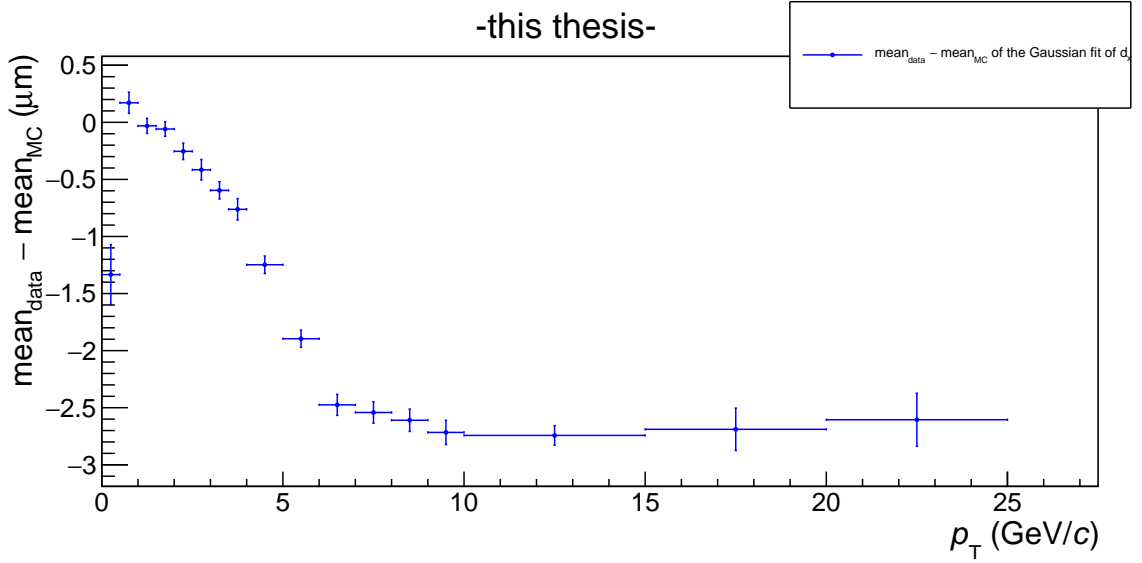
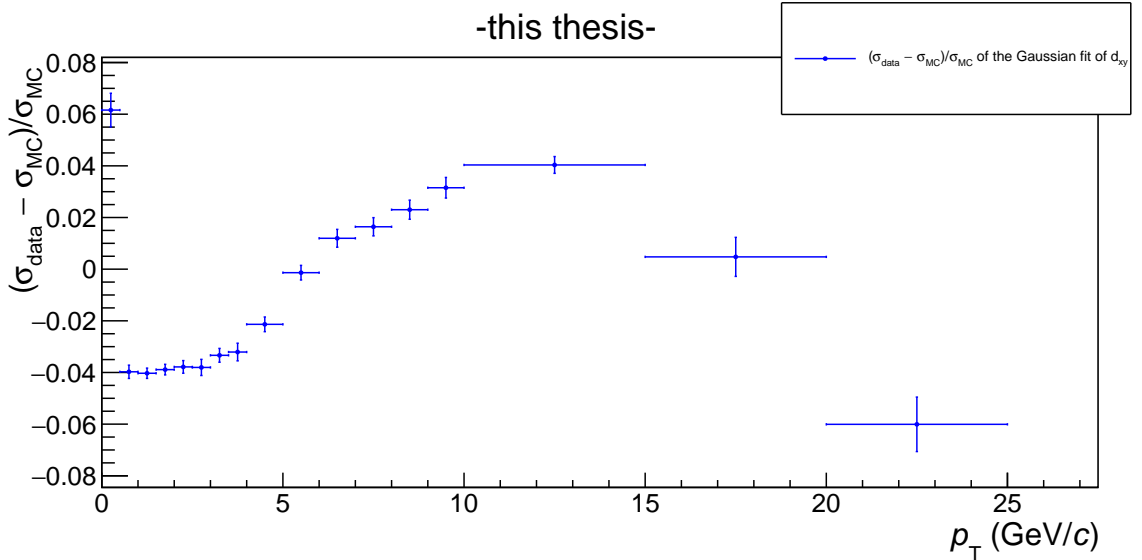


Figure 26: Comparison of the Gaussian standard deviations of the  $d_{xy}$  distributions from data and MC in p–Pb collisions at  $\sqrt{s_{NN}} = 5.02$  TeV.

Furthermore, the compatibility of the fit parameters was investigated in dependence of  $p_T$  which is shown in Fig. 27. In Fig. 27a the mean of the Gaussian fit for data is subtracted by the mean of the Gaussian fit for MC while in the lower figure the difference between the standard deviations for data and MC is divided by  $\sigma$  for MC in dependence of  $p_T$ . For  $p_T \leq 4$  GeV/ $c$  the means deviate less than  $1.5 \mu\text{m}$  and approximately  $2.5 \mu\text{m}$  for higher  $p_T$ . Furthermore, as shown in Fig. 27b, the standard deviations of the Gaussian fits deviate less than 8 % over the full range in  $p_T$ .



(a) Difference between the means of the Gaussian fits of the  $d_{xy}$  distributions from data and MC in dependence of  $p_T$  in p–Pb collisions at  $\sqrt{s_{NN}} = 5.02$  TeV.



(b) Difference of the standard deviations of the Gaussian fits of the  $d_{xy}$  distributions from data and MC in units of  $\sigma_{MC}$  in dependence of  $p_T$  in p–Pb collisions at  $\sqrt{s_{NN}} = 5.02$  TeV.

Figure 27: Compatibility of the Gaussian fit parameters of the  $d_{xy}$  distributions from data and MC in dependence of  $p_T$  in p–Pb collisions at  $\sqrt{s_{NN}} = 5.02$  TeV.

Also a cross check was performed whose results are shown in the appendix in Chapter 9. For  $p_T$  larger than 15 GeV/ $c$  cross check and Gaussian method deviate because the Gaussian fit worsens due to decreasing number of entries.

## 6.2 Angular dependence

Furthermore, the  $d_{xy}$  distribution was analyzed to approve angular independence. The  $d_{xy}$  distribution was divided into two bins of equal width for  $\eta$  and four bins

of equal width for  $\phi$ . Then the respective bins were analyzed as in Chapter 6.1 and the fit results of the Gaussian fits were compared. An example is shown in Fig. 28 where the difference of the mean of the Gaussian for data is shown for a comparison of different  $\eta$  and  $\phi$  bins.

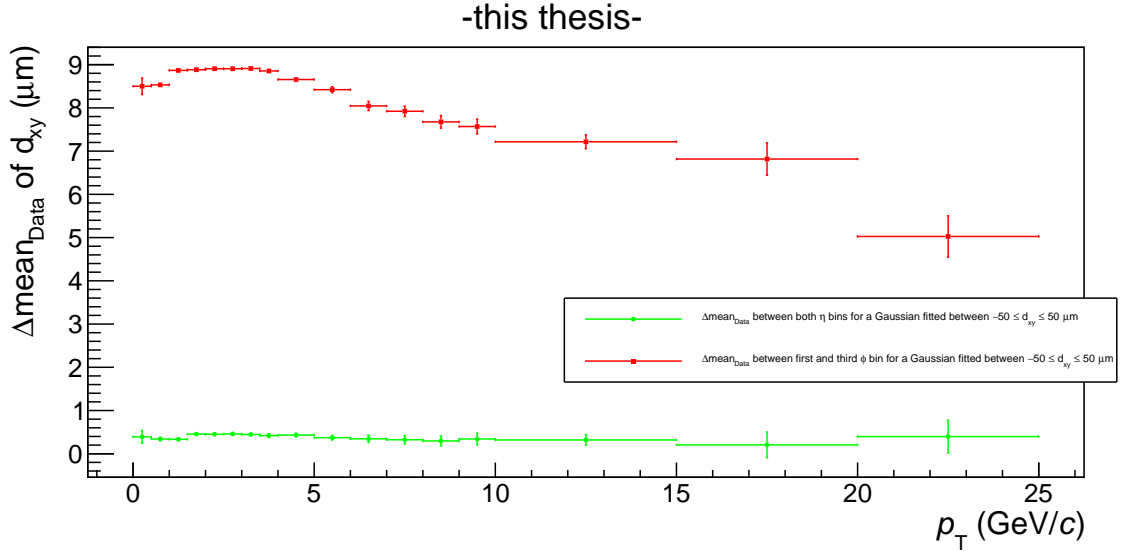


Figure 28: Comparison of the mean of the Gaussian from data for various bins for polar and azimuthal angle in dependence of  $p_T$  in p–Pb collisions at  $\sqrt{s_{\text{NN}}} = 5.02$  TeV.

The mean of the Gaussian from data deviates  $0.41 \mu\text{m} \pm 2.4 \%$  between both eta bins. First and third azimuthal angle bin deviate  $8.78 \mu\text{m} \pm 1.5 \%$  for  $0 \leq p \leq 5$  GeV/c. Consequently the impact parameter distribution is depending on  $\phi$  but independent of  $\eta$ . A possible explanation was that the collisions were shifted from the nominal collision point in the  $xy$ -plane-

### 6.3 Conclusion and impact parameter cut

Even though the MC was already worsened to match the data it does not yet represent the data sufficient and a small correction has to be applied to remove the deviations of the means of the  $d_{xy}$  distributions from data and MC. Furthermore, the azimuthal angle dependency has to be removed. In order to reduce the hadron contamination and separate the electrons from beauty-hadron decays a selection on the impact parameter was applied. Since S/B and width of the impact parameter distribution depend on  $p_T$  the impact parameter cut is also  $p_T$  dependent. Because S/B of electrons originating from beauty-hadron decays increases for large impact parameter only left and right tail of the  $d_{xy}$  distribution are used for further analysis. The same cut as in [3] was applied which was determined by Monte Carlo simulations to maximize the significance of electrons originating from beauty-hadron decays [3]. Thus, electron candidates with an impact parameter  $|d_{xy}| > 0.0054 + 0.078 \cdot \exp(-0.56 \cdot p_T)$  were selected. In this equation the impact parameter is given in cm and  $p_T$  in GeV/c.

## 7 Electron background

In order to separate electrons that originate from beauty-hadron decays, background sources have to be subtracted from the inclusive electron yield. In general, there are 3 types of background electrons such as electrons originating from conversion processes, electrons coming from Dalitz decays and electrons originating from charm-hadron decays. In addition, there is hadron contamination caused by charged kaons, charged pions and protons from the primary vertex or protons originating from decays of  $\Sigma$  or  $\Lambda$  baryons. In general,  $\pi^0$  decays are the largest contribution to background and includes electrons coming directly from the decay and electrons coming from conversion caused by the interaction of decay photons with the detector material. Electrons originating from decays of light neutral mesons such as  $\pi^0$ ,  $\eta$ ,  $\eta'$ ,  $\rho$ ,  $\omega$  and  $\phi$  are called Dalitz electrons. They are produced close to the primary vertex due to their short decay length and therefore their decay vertex cannot be distinguished from the primary vertex within the detector resolution. Photons created in decays, for example  $\pi^0$ , with a branching ratio of  $\pi^0 \rightarrow \gamma\gamma \approx 98.823\%$  [3], interact with the detector material creating conversion electrons ( $\gamma \rightarrow e^+e^-$ ). Since hits in both pixel layers of the SPD are required, only electrons coming from conversion in the beam pipe or the first layer contribute to the electron sample. Furthermore, there are strange-hadron decays of  $K_S^0$ ,  $K$  mesons and  $\Lambda$  baryons which decay into  $\pi^0$  and therefore contribute to the same background sources as  $\pi^0$ . Due to the impact parameter cut the importance of electrons coming from secondary decays of  $\pi^0$  increases and is comparable with the one from primary decays [3]. The idea is to remove background sources of electrons coming from conversions, and Dalitz decays by using the MC truth information. By multiplying the identified particle yields in MC by a transverse momentum dependent “weighting factor”, the scaled identified particle yields from the MC correspond to the particle yields in data. Since in the MC the origin of each detected particle is known from the MC truth information. The contamination of the electron yield after applying the selection criteria can be directly identified. Because all particle yields are calculated per event, the contamination is extracted in percent of the inclusive electron spectrum and therefore the background sources is directly subtracted from the inclusive electron spectrum in data. For this reason, the identified particle yields in data have to be obtained. The particle yields of various background sources were taken from other ALICE measurements in p–Pb at  $\sqrt{s_{NN}} = 5.02$  TeV where the corresponding yields had been analyzed in multiplicity bins. All yields were multiplied and  $2\pi p_T$  and by the multiplicity bin width for normalization. Electrons coming from charm-hadron decays were separated by usage of the kinematic distribution for  $D$ -mesons derived from [49] since the selection criteria are equal to the selection criteria performed in this analysis. The relative importance of the respective background sources strongly depends on the transverse momentum [13]. In the  $p_T$  interval of  $0.1 - 0.9$  GeV/ $c$  the background spectrum is dominated by electrons originating from conversion and Dalitz decays. Electrons originating from charm-hadron decays dominate the background source spectrum in range of transverse momentum of  $0.9 - 5.5$  GeV/ $c$ . For transverse momenta above  $5.5$  GeV/ $c$  hadron contamination is the most important background source.

## 7.1 Subtraction of the background sources

Data was taken from [47] for  $\pi^\pm, K^\pm, K_S^0$  and  $\Lambda$  from [50] where the transverse momentum dependencies of the particle yields were studied for various multiplicity bins. Charged pions were used because no measurement for the respective neutral meson existed while this analysis was performed and it is assumed that the neutral pions have the same particle yields as their charged counterparts which is based on symmetry arguments ( $N_{\pi^0} = (N_{\pi^-} + N_{\pi^+})/2$ ). The background contribution created by light neutral mesons,  $K^\pm$  mesons and  $\Lambda$  baryons was estimated by a cocktail approach. For this, the kinematic distributions were taken from HEPData or obtained by  $m_T$ -scaling of the kinematic distribution of charged pions from [47]. Because the charged pion distribution is described best and is the largest single electron background source, its particle yield was used as the reference spectrum. This particle yield can be described by a Tsallis distribution [48]. In Fig. 29 the  $p_T$  dependent pion yield divided by the number of events is shown which is fitted with a Tsallis function colored in red.

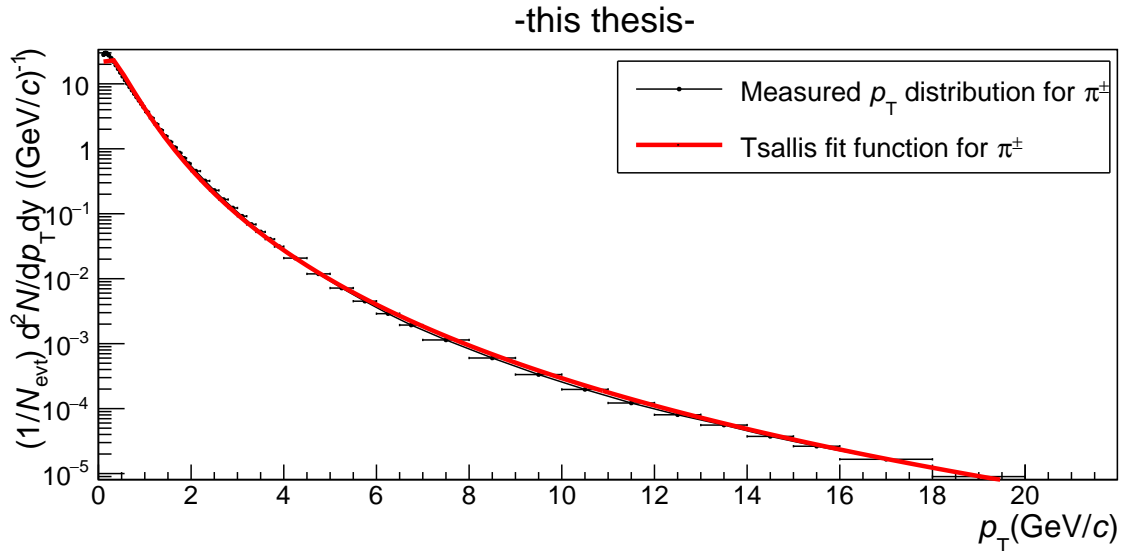


Figure 29: Transverse momentum dependent particle yield of charged pions  $(\pi^+ + \pi^-)/2$  at mid-rapidity fitted with a Tsallis function in p–Pb collisions at  $\sqrt{s_{NN}} = 5.02$  TeV.

How much data and the Tsallis function deviate can be seen in Fig. 30 where the data values are divided by the respective value of the Tsallis function. The average ratio is 0.93 with a standard deviation of 9%. For heavier particles, such as  $\eta', \rho, \omega$  and  $\phi$ , where no data was available, this Tsallis function was used as reference parameterization for  $m_T$ -scaling in order to obtain the respective kinematic distribution. The  $m_T$ -scaling is based on the parameter  $m_T = \sqrt{p_T^2 + m_0^2}$  where one assumes that the invariant particle yields differentiated by transverse momentum or transverse mass are equal [46]:

$$\frac{1}{p_T} \frac{d^2N}{dp_T dy} = \frac{1}{m_T} \frac{d^2N}{dm_T dy} \quad (8)$$

At mid-rapidity the invariant  $p_T$  spectrum of a particle can thus be obtained by scaling the parameterization of the kinematic distribution of a reference particle [46] which is  $\pi^0$  in this thesis. Because no kinematic distribution exists for  $\eta'$ ,  $\rho$ ,  $\omega$  and  $\phi$ , the Tsallis function obtained for the charged pions was  $m_T$ -scaled. An example can be seen in Fig. 31 where the yield of  $\eta'$  is shown as a function of  $p_T$ .

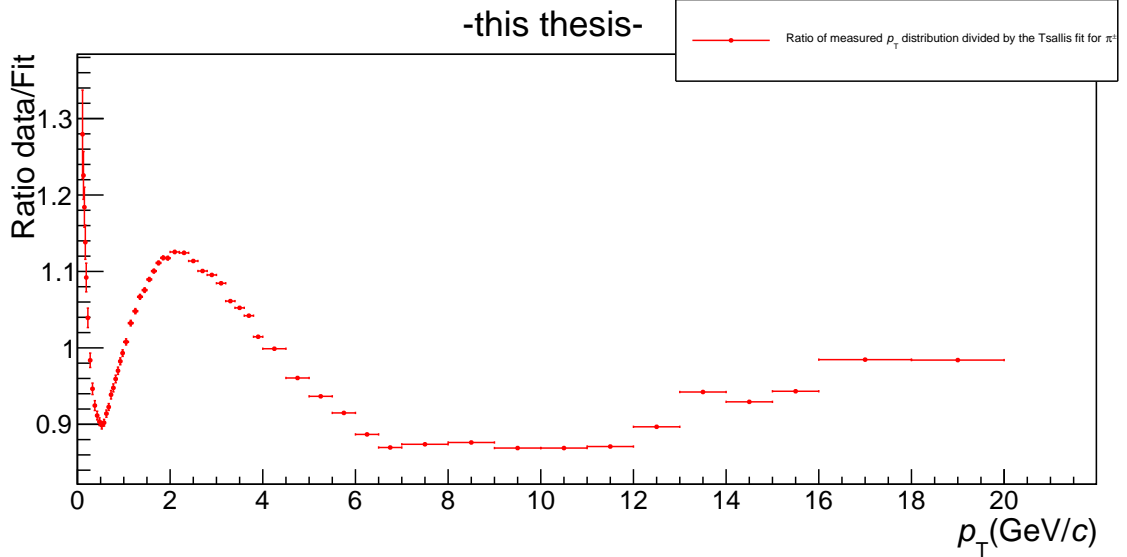


Figure 30: Ratio of measured  $p_T$  distribution for charged pions  $((\pi^+ + \pi^-)/2)$  and the corresponding Tsallis fit function in p–Pb collisions at  $\sqrt{s_{NN}} = 5.02$  TeV.

In order to subtract conversion and Dalitz electrons, the transverse momentum distributions were compared to the respective distributions from the MC. Because the particle yields in data differ strongly from the particle yield from the MC, the kinematic distribution of the background cocktail has to be scaled by “weighting factors” as explained above. Afterwards the background cocktail can be subtracted from the inclusive spectrum. How the “weighting factors” were calculated is shown, for instance, for  $\pi^0$  in Fig. 32. In the left figure the  $p_T$  distribution of  $\pi^0$  for data (colored in red) and for MC (represented in blue) are shown. By division of the particle yields in data and MC, the  $p_T$  dependent “weighting factor” is obtained which is shown for  $\pi^0$  in the right figure. This was done for each background component and subtracted from the inclusive electron spectrum.

Because the same selection criteria as in the ALICE Analysis Note from 2013 [49] explained in Chapter 5 and 6 were applied, the background from hadron contamination and the contribution of electrons from charm-hadron decays can be calculated. By subtraction of the background sources from the inclusive spectrum after track and event selection, eID and requirement of the impact parameter, the raw  $b \rightarrow e$  spectrum was obtained which is shown in Fig. 33 with the inclusive spectrum and various background sources as a function of transverse momentum. Even though a selection was applied on the impact parameter and on the  $N_{\sigma_{\text{electron}}^{\text{TPC}}}$  distribution there is still contamination caused by protons which is about 10 % (4 %) in the  $p_T$  interval  $1.0 \leq p \leq 1.1$  GeV/ $c$  ( $1.1 \leq p \leq 1.2$  GeV/ $c$ ) [3].

As pointed out above, conversion and Dalitz electrons are the main background sources for transverse momenta below 0.9 GeV/ $c$ . For higher transverse momenta

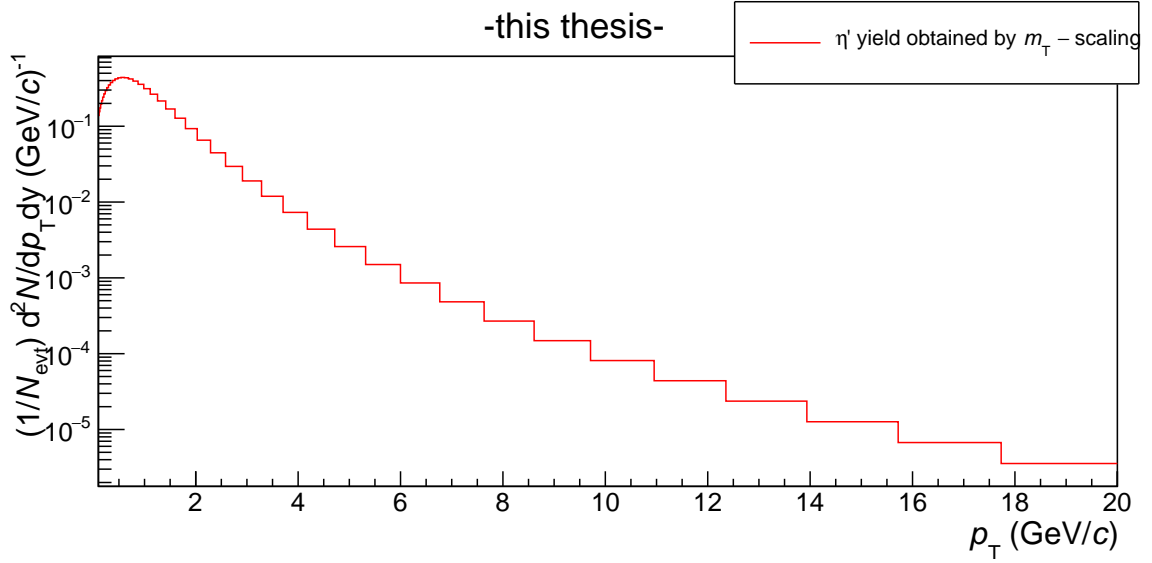


Figure 31:  $\eta'$  yield obtained by  $m_T$ -scaling of the Tsallis fit function of charged pions in p–Pb collisions at  $\sqrt{s_{NN}} = 5.02$  TeV.

it is exceeded by the contribution of electrons coming from charm-hadron decays which is dominant until 5.5 GeV/c from where on the hadron contamination dominates. Below 0.7 GeV/c the amount of electrons originating from beauty-hadron decays is smaller than the 3 background sources combined, especially due to electrons coming from conversion and electrons coming from Dalitz decays. In the range of 0.7 until 1.2 GeV/c the share of electrons coming from charm-hadron decays from the inclusive spectrum increases. For momenta between 1.2 to 1.4 GeV/c the contribution of electrons originating from beauty-hadron decays and electrons coming from charm-hadron decays are approximately equal. Furthermore the signal-to-background ratio in this region is approximately 1/3. It increases for increasing momentum until the maximum S/B of approximately 5.8 is reached between 4 and 4.5 GeV/c where the hadron contamination becomes important. Furthermore, for momenta above 4.5 GeV/c the S/B decreases again due to the increasing hadron contamination. The goal of this analysis is to correct this spectrum in terms of geometrical acceptance (pseudorapidity and  $\phi$  dependence), eID, reconstruction efficiency and impact parameter selection efficiency which is not done in this thesis but is described in the outlook in Chapter 8.

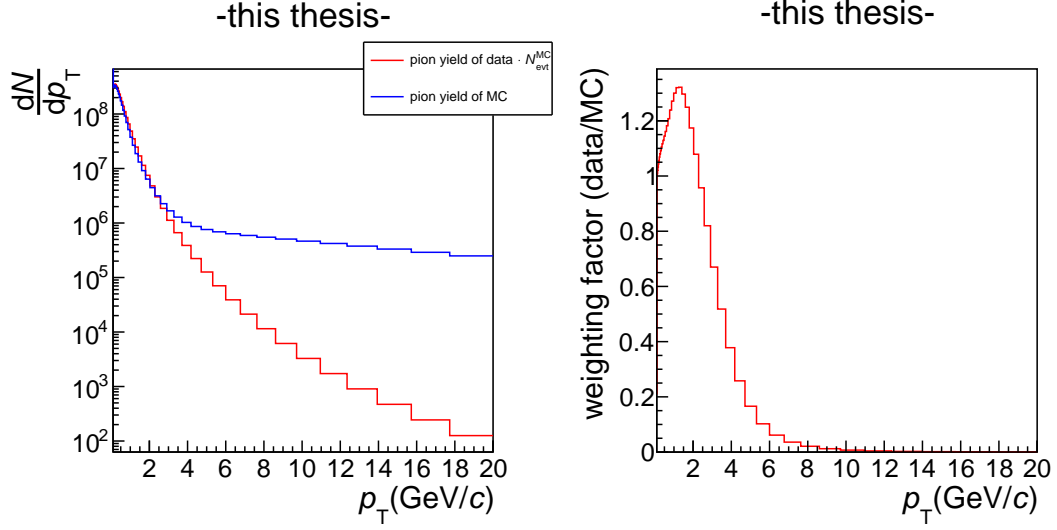


Figure 32: Calculation of the weighting factor for  $\pi^0$  in p–Pb collisions at  $\sqrt{s_{\text{NN}}} = 5.02$  TeV.

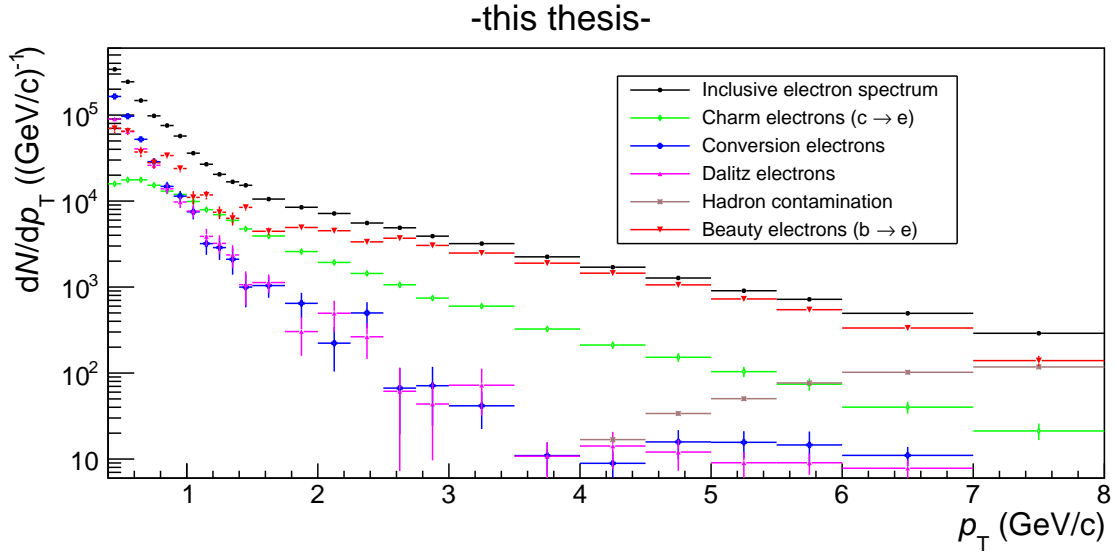


Figure 33: Signal and background yields of electrons from various sources after the impact parameter cut in p–Pb collisions at  $\sqrt{s_{\text{NN}}} = 5.02$  TeV.

## 8 Discussion, summary and outlook

In this thesis the raw  $p_T$ -dependent yield of electrons originating from beauty-hadron decays in minimum-bias p–Pb collisions at  $\sqrt{s_{NN}} = 5.02$  TeV was measured. First the  $N_{\sigma_{electron}^{TOF}}$  distribution and the  $N_{\sigma_{electron}^{TPC}}$  distribution were inspected by projections in momentum slices which were fitted by Gaussian functions. The electron candidates were separated from other charged particles in range of  $|N_{\sigma_{electron}^{TOF}}| \leq 3$  and  $-0.5 \leq N_{\sigma_{electron}^{TPC}} \leq 3$  with an efficiency of 69 %. A pseudorapidity dependence of the  $N_{\sigma_{electron}^{TPC}}$  distribution was observed, as well as the dependence of the  $d_{xy}$  distribution on the momentum and on the azimuthal angle. Furthermore the signal-to-background ratio of electrons from beauty-hadron decays was enhanced by a selection on the impact parameter. With the  $N_{\sigma_{electron}^{TPC}}$  selection the hadron contamination was reduced to maximum 15.4 % at 8 GeV/ $c$ . The rest of the electron background was subtracted from the inclusive spectrum by a cocktail approach where the various particle yields from the MC were re-weighted to match the particle yields from data. The data for the various background sources of the background cocktail was obtained from other ALICE measurements or by  $m_T$ -scaling. Then the various background sources were subtracted and the uncorrected raw  $p_T$  yield, which was divided by the number of events, of electrons originating from beauty-hadron decays was obtained. Target of this analysis is the corrected  $p_T$  spectrum of electrons from beauty-hadron decays with estimated uncertainties. Thus, the raw yield has to be corrected for geometrical acceptance and the efficiency of the track reconstruction, TOF electron identification, TPC electron identification, proton contribution in the  $p_T$  interval  $1.0 \leq p_T \leq 1.2$  and impact parameter cut selection. Furthermore the systematic uncertainties have to be estimated by repetition of the analysis with modified selection criteria such as track selection and eID selection. After this the results will be compared to the results of the ALICE Analysis Note 2013 [49]. Finally, the corrected yield with estimated uncertainties of electrons from beauty-hadron decays will be used to estimate cold nuclear matter effects. Then the determined effects will be used to analyze hot nuclear matter effects in Pb–Pb collisions to study the interaction of QCD probes with the QGP and characterize its properties.

## 9 Appendix

Logistic growth fit

$$f(x) = \frac{0.284}{\exp(-4.46 \cdot (|x+0.038|-0.459)) + 1} - 0.0654 \quad (9)$$

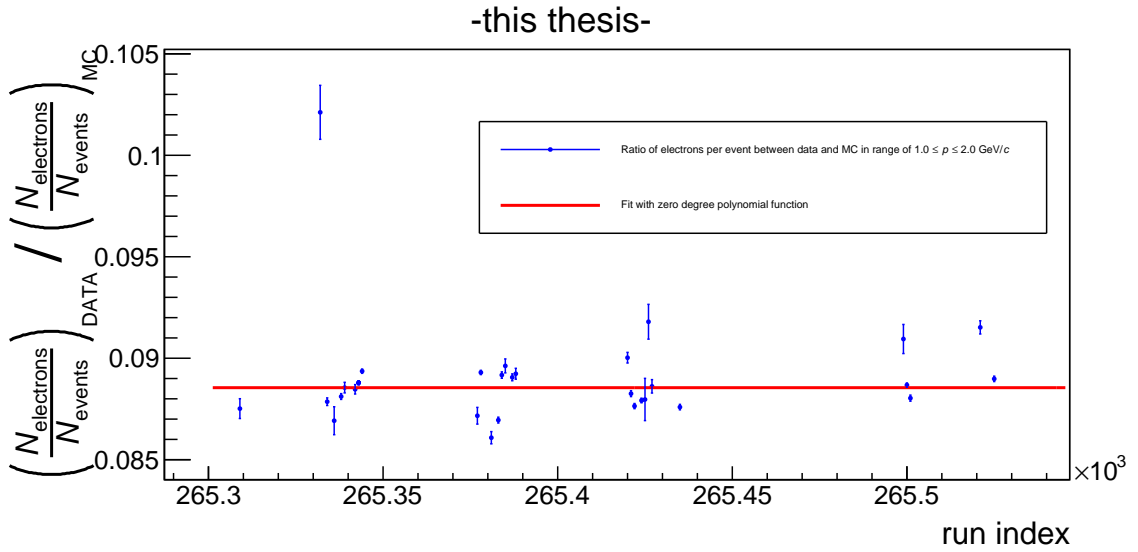


Figure 34:  $\left(\frac{N_{electrons}}{N_{events}}\right)_{data} / \left(\frac{N_{electrons}}{N_{events}}\right)_{MC}$  in the momentum range of  $1.0 \leq p \leq 2.0$  GeV/c in p–Pb collisions at  $\sqrt{s_{NN}} = 5.02$  TeV.

The ratio between data and MC for the amount of electrons per event in momentum range of  $1.0 \leq p \leq 2.0$  GeV/c is described by the value of approximately  $0.088 \pm 0.03$  % electrons per event scaled by bin width and momentum width ( $\chi^2_{red} = 27$ ). The value for run index 265332 deviates significantly from the others since for this run index exists only a total of 414769 events for data and 7613 events for MC which explains the sensitivity towards statistical fluctuations.

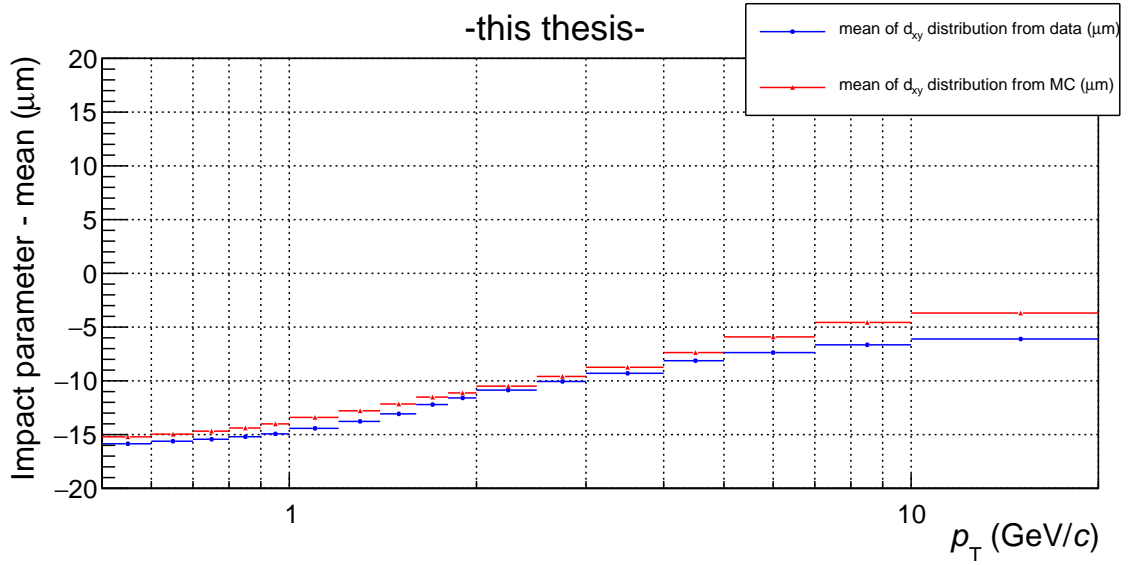


Figure 35: cross check mean  $d_{xy}$  in p–Pb collisions at  $\sqrt{s_{NN}} = 5.02$  TeV.

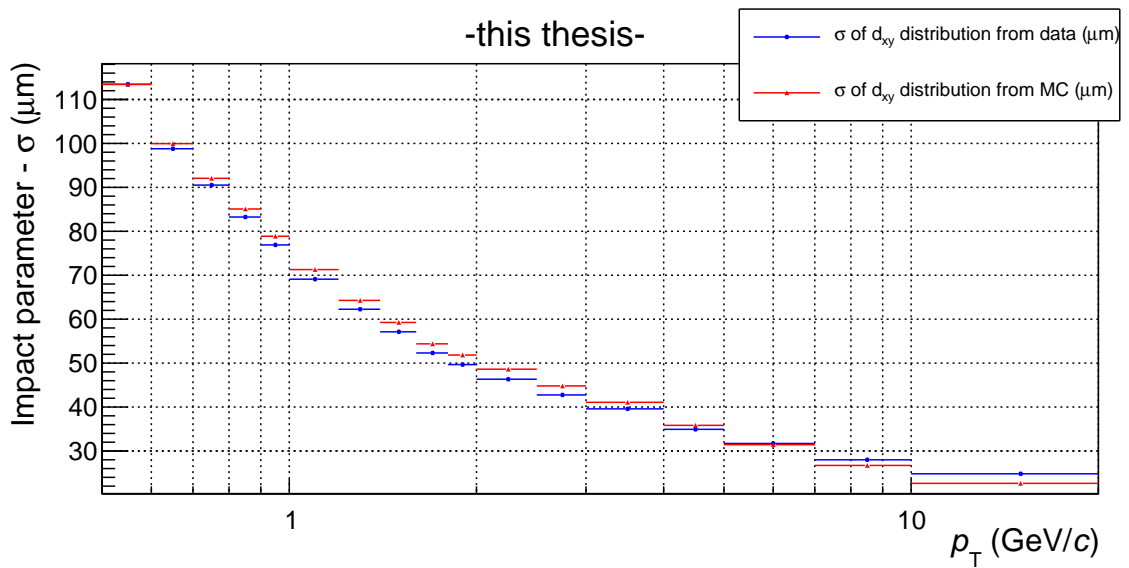


Figure 36: cross check  $\sigma d_{xy}$  in p–Pb collisions at  $\sqrt{s_{NN}} = 5.02$  TeV.

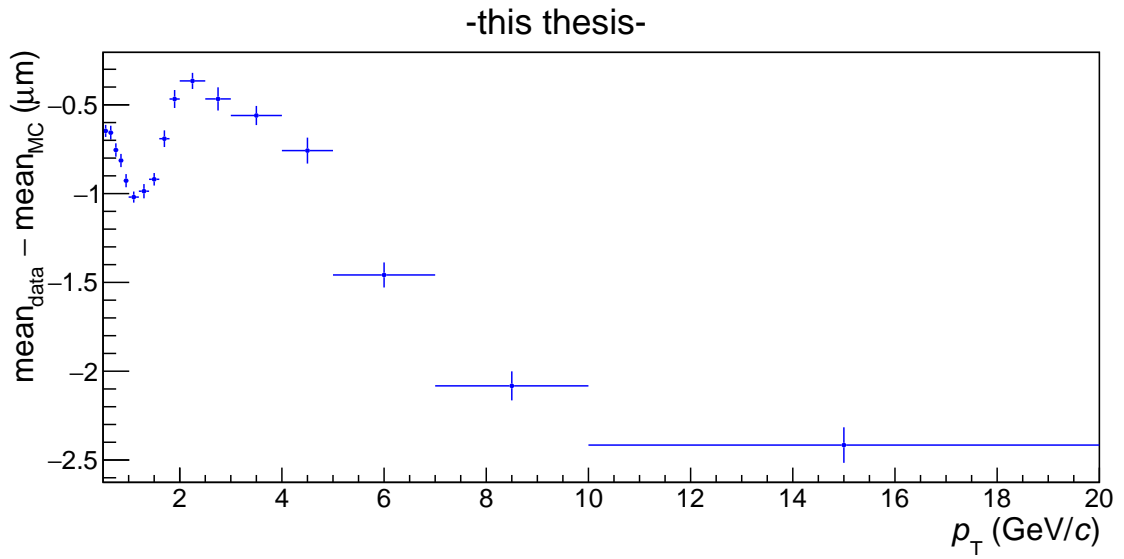


Figure 37: cross check  $\Delta_{\text{mean}} d_{xy}$  in p–Pb collisions at  $\sqrt{s_{\text{NN}}} = 5.02$  TeV.

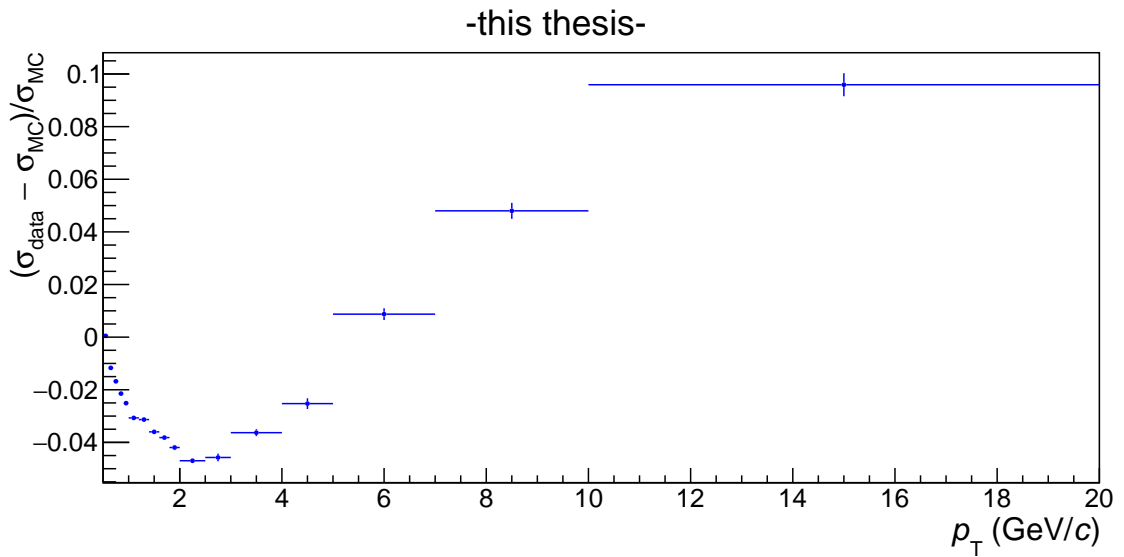


Figure 38: cross check  $\sigma_{\text{ratio}} d_{xy}$  in p–Pb collisions at  $\sqrt{s_{\text{NN}}} = 5.02$  TeV.

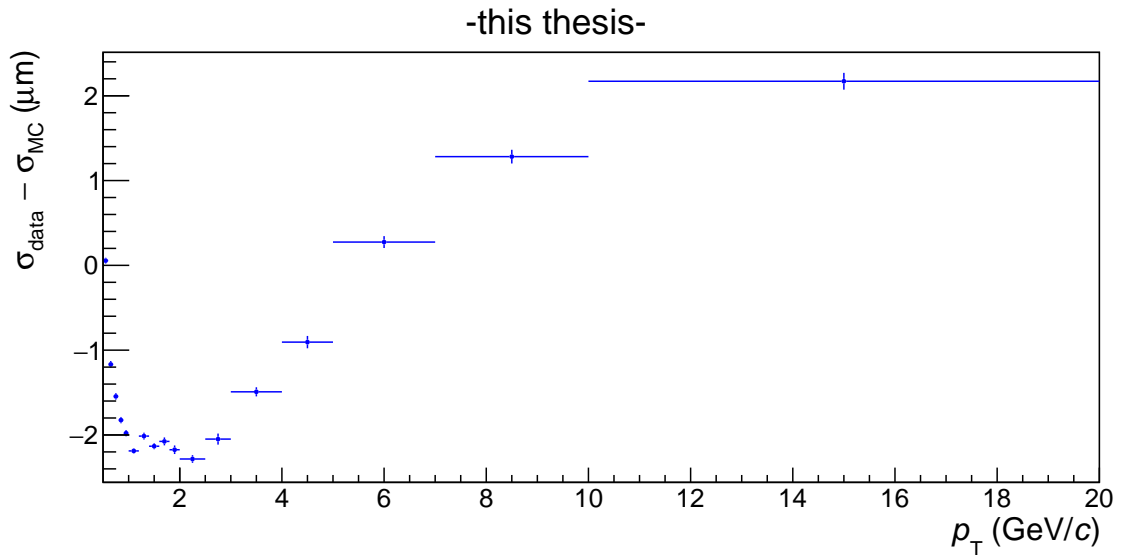


Figure 39: cross check  $\Delta_\sigma d_{xy}$  in p–Pb collisions at  $\sqrt{s_{\text{NN}}} = 5.02$  TeV.

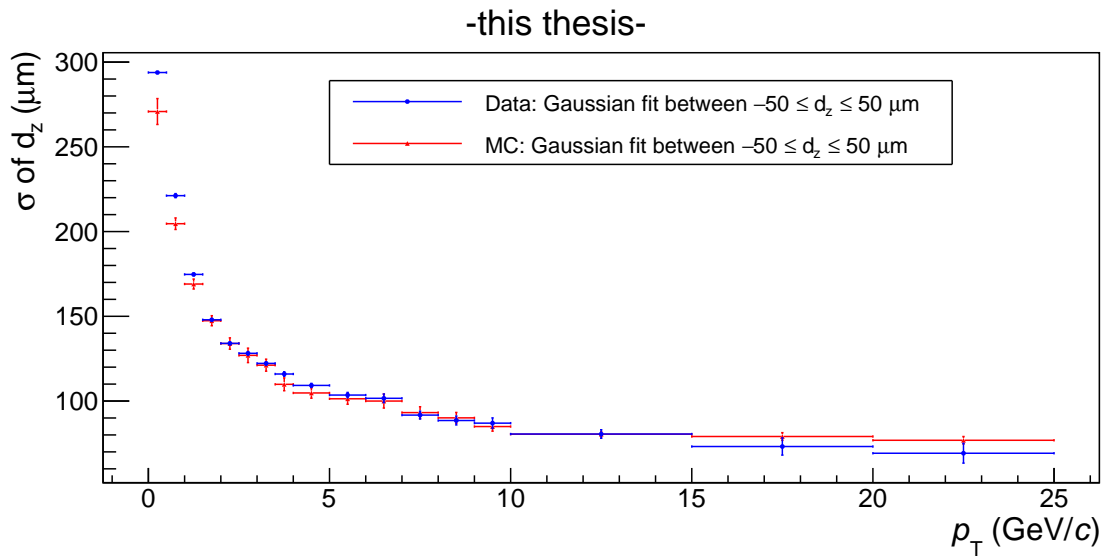


Figure 40: standard deviation  $d_z$  in p–Pb collisions at  $\sqrt{s_{\text{NN}}} = 5.02$  TeV.

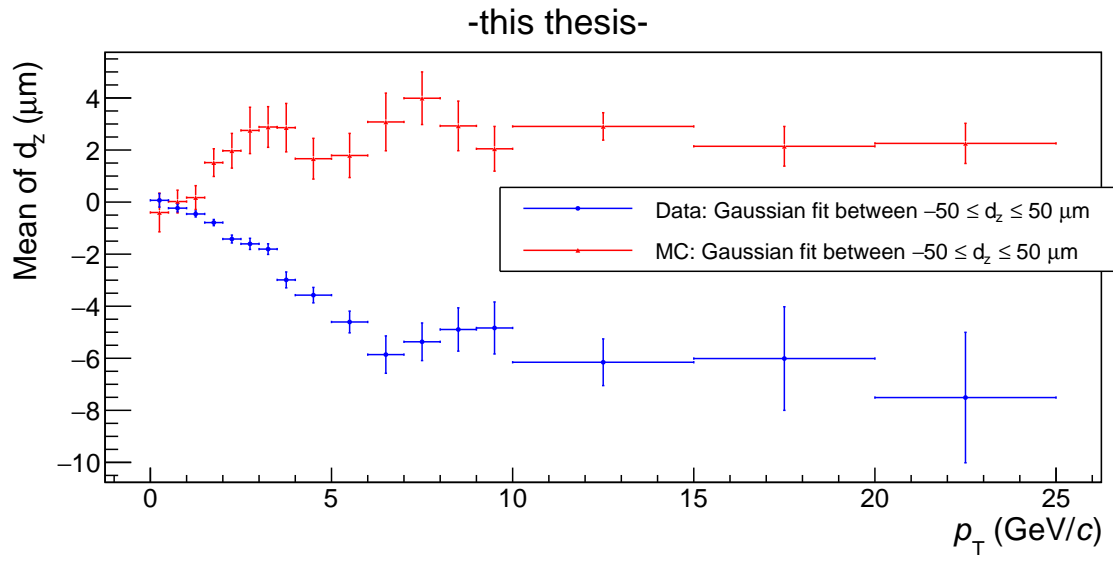


Figure 41: mean  $d_z$  in p–Pb collisions at  $\sqrt{s_{\text{NN}}} = 5.02$  TeV.

## References

- [1] M. Knichel. “Transverse momentum distribution of primary charged particles in pp, p-Pb and Pb-Pb collisions measured with ALICE at the LHC.” Dissertation (TU Darmstadt,2014): 45-53. URL: [http://tuprints.ulb.tu-darmstadt.de/4930/1/mknichel\\_dissertation.pdf](http://tuprints.ulb.tu-darmstadt.de/4930/1/mknichel_dissertation.pdf)
- [2] J. Adam et al. (ALICE Collaboration). “Measurement of electrons from heavy-flavor hadron decays in p-Pb collisions at 5.02 TeV.” arXiv preprint arXiv:1509.07491 (2015). URL: <https://arxiv.org/pdf/1509.07491.pdf>
- [3] Y. Pachmayer et al. (ALICE Collaboration). “Measurement of electrons from beauty-hadron decays in p-Pb collisions at 5.02 TeV and Pb-Pb collisions at 2.76 TeV.” arXiv preprint arXiv:1609.03898 (2016). URL: <https://arxiv.org/pdf/1609.03898.pdf>
- [4] B. Abelev et al. (ALICE Collaboration). “Transverse Momentum Distribution and Nuclear Modification Factor of Charged Particles in  $p + \text{Pb}$  Collisions at  $\sqrt{s_{\text{NN}}}=5.02$  TeV.” Phys. Rev. Lett. 110, 082302 (2013). URL: <https://journals.aps.org/prl/pdf/10.1103/PhysRevLett.110.082302>
- [5] J. Beringer et al. (Particle Data Group). “REVIEW OF PARTICLE PHYSICS.” Phys. Rev. Lett. D 86, 010001 (2012). URL: <https://journals.aps.org/prd/pdf/10.1103/PhysRevD.86.010001>
- [6] K. Nakamura et al. (Particle Data Group). “REVIEW OF PARTICLE PHYSICS.” Phys. Rev. Lett. G 37, 075021 (2010). URL: <http://pdg.lbl.gov/2010/download/rpp-2010-JPhys-G-37-075021.pdf>
- [7] A. Kalweit et al. (ALICE TPC Collaboration). “Astroparticle, Particle, Space Physics, Radiation Interaction, Detectors and Medical Physics Applications.” (2010) Book 54-58. URL: [https://doi.org/10.1142/9789814307529\\_0009](https://doi.org/10.1142/9789814307529_0009)
- [8] B. Abelev et al. (ALICE Collaboration). “Performance of the ALICE experiment at the CERN LHC.” arXiv preprint arXiv:1402.4476 (2014) URL: <https://arxiv.org/pdf/1402.4476.pdf>
- [9] J. Wiechula. “Commissioning and Calibration of the ALICE-TPC.” Dissertation (2008): 15-23. URL: [https://www.uni-frankfurt.de/46491136/PHDThesis\\_Jens\\_Wiechula.pdf](https://www.uni-frankfurt.de/46491136/PHDThesis_Jens_Wiechula.pdf)
- [10] P. Hanus. “Entropy in Pb-Pb Collisions at the LHC.” Bachelorthesis (2018) 5-10. URL: [https://www.physi.uni-heidelberg.de/Publications/Bachelor\\_Thesis\\_Patrick\\_Hanus\\_2018.pdf](https://www.physi.uni-heidelberg.de/Publications/Bachelor_Thesis_Patrick_Hanus_2018.pdf)
- [11] P. Rosnet. “Quark-Gluon Plasma: from accelerator experiments to early Universe” arXiv preprint arXiv:1510.04200 (2015). URL: <https://arxiv.org/pdf/1510.04200.pdf>

- [12] U. Uwer. Physik V, Kapitel VII-a, Starke Wechselwirkung 2006. URL: <https://www.physi.uni-heidelberg.de/~uwer/lectures/PhysikV/Vorlesung/Kapitel-VIIa.pdf>
- [13] M. Völkl. “Electrons from beauty-hadron decays in central Pb–Pb collisions at  $\sqrt{s_{NN}} = 2.76$  TeV.” Dissertation (Uni Heidelberg, 2016) URL: [https://www.physi.uni-heidelberg.de//Publications/Thesis\\_Voelkl.pdf](https://www.physi.uni-heidelberg.de//Publications/Thesis_Voelkl.pdf)
- [14] C. Shen (Brookhaven National Lab). Hydrodynamics in Small Collision Systems from LHC to RHIC (2017). URL: [https://www.bnl.gov/aum2017/content/workshops/Workshop\\_1e/Shen\\_small\\_systems\\_UsersMeeting2017.pdf](https://www.bnl.gov/aum2017/content/workshops/Workshop_1e/Shen_small_systems_UsersMeeting2017.pdf)
- [15] A. Adare et al. (PHENIX Collaboration). Cold-Nuclear-Matter Effects on Heavy-Quark Production at Forward and Backward Rapidity in d + Au Collisions at  $\sqrt{s_{NN}} = 200$  GeV. URL: [https://www.bnl.gov/aum2017/content/workshops/Workshop\\_1e/Shen\\_small\\_systems\\_UsersMeeting2017.pdf](https://www.bnl.gov/aum2017/content/workshops/Workshop_1e/Shen_small_systems_UsersMeeting2017.pdf)
- [16] M. Ivanov et al. (ALICE Collaboration). “The ALICE Transition Radiation Detector: construction, operation, and performance” arXiv preprint arXiv:1709.02743 (2017). URL: <https://arxiv.org/pdf/1709.02743.pdf>
- [17] M. Ivanov et al. (ALICE Collaboration). ALICE tracking system. (2014) URL: <https://indico.gsi.de/event/2715/session/0/contribution/3/material/slides/0.pdf>
- [18] L. Betev et al. (ALICE Collaboration). “Definition of the ALICE Coordinate System and Basic Rules for Sub-detector Components Numbering.” (2003) URL: [https://alice-servotech.web.cern.ch/ALICE-ServoTech/HELP\\_DCDB-SVT/Help\\_Files/ALICE-INT-2003-038.pdf](https://alice-servotech.web.cern.ch/ALICE-ServoTech/HELP_DCDB-SVT/Help_Files/ALICE-INT-2003-038.pdf)
- [19] ALICE. The ALICE Time of Flight Detector (2008). URL: [http://aliceinfo.cern.ch/Public/en/Chapter2/Chap2\\_TOF.html](http://aliceinfo.cern.ch/Public/en/Chapter2/Chap2_TOF.html)
- [20] Y. Pachmayer. Physikalisches Institut, Im Neuenheimer Feld 226, 69120 Heidelberg, Germany
- [21] A. Alici et al. (ALICE Collaboration). “Status and performance of the ALICE MRPC-based Time-Of-Flight detector.” JINST 7 P10024 (2012). URL: <http://iopscience.iop.org/article/10.1088/1748-0221/7/10/P10024/pdf>
- [22] L. Altenkämper. “Measurement of Direct Photons in Proton-Proton Collisions at  $\sqrt{s} = 7$  TeV with ALICE.” Masterthesis (2016). URL: [https://www.physi.uni-heidelberg.de//Publications/thesis\\_altenkaemper\\_19122016.pdf](https://www.physi.uni-heidelberg.de//Publications/thesis_altenkaemper_19122016.pdf)
- [23] ALICE. V0 detector (2014). URL: <http://alice.web.cern.ch/content/v0-detector>
- [24] M. Keller et al. (ALICE Collaboration). “ALICE Technical Design Report of the Time Projection Chamber.” (2000). URL: <https://cds.cern.ch/record/451098/files/open-2000-183.pdf>

- [25] B. Alessandro et al. (ALICE Collaboration). “ALICE: Physics Performance Report, Volume II.” J. Phys. G: Nucl. Part. Phys. 32 1295 (2006) URL: <http://iopscience.iop.org/article/10.1088/0954-3899/32/10/001/pdf>
- [26] M. Heide. “Measurement of Semi-Electronic Beauty-Hadron Decays via their Impact Parameter in pp Collisions in ALICE” Dissertation (Uni Münster, 2014). URL: [https://www.uni-muenster.de/imperia/md/content/physik\\_kp/agwessels/thesis\\_db/ag\\_wessels/heide\\_2014\\_dissertation.pdf](https://www.uni-muenster.de/imperia/md/content/physik_kp/agwessels/thesis_db/ag_wessels/heide_2014_dissertation.pdf)
- [27] Particle Data Group. “Quantum Chromodynamics.” (2017). URL: <http://pdg.lbl.gov/2018/reviews/rpp2018-rev-qcd.pdf>
- [28] Gottfried Weisskopf, Concepts of Particle Physics, Vol. 1, Oxford University Press
- [29] J. Stachel et al. QGP Physics - From Fixed-Target to LHC: 4. Thermodynamics of the QGP (SS 2011). URL: [https://www.physi.uni-heidelberg.de/~reygers/lectures/2011/qgp/qgp\\_04\\_thermo.pdf](https://www.physi.uni-heidelberg.de/~reygers/lectures/2011/qgp/qgp_04_thermo.pdf)
- [30] Y. Dokshitzer. “QCD and Hadron Dynamics.” arXiv preprint arXiv:10106348v1 (2001). URL: <https://arxiv.org/pdf/hep-ph/0106348.pdf>
- [31] P. Preuss et al. (BERKELEY LAB). When Matter Melts (2011). URL: <https://sciencenode.org/feature/when-matter-melts.php>
- [32] K. Schweda. “Prompt production of D mesons with ALICE at the LHC.” Habilitation (2013). URL: <https://arxiv.org/pdf/1402.1370.pdf>
- [33] R. Arnaldi. (Heavy) Flavour production and the QGP in heavy ion collisions (2017). URL: [https://indico.cern.ch/event/466934/contributions/2474213/attachments/1491539/2318871/EPS2017\\_Arnaldi\\_plenary.pdf](https://indico.cern.ch/event/466934/contributions/2474213/attachments/1491539/2318871/EPS2017_Arnaldi_plenary.pdf)
- [34] Y. Gorbunov. Strangeness production in a Quark Gluon Plasma (2010) URL: <https://www.star.bnl.gov/~gorbunov/main/node5.html>
- [35] M. Peskin et al. “An introduction to quantum field theory.” (1995) URL: [http://www.fulviofrisone.com/attachments/article/483/Peskin,%20Schroesder%20-%20An%20introduction%20To%20Quantum%20Field%20Theory\(T\).pdf](http://www.fulviofrisone.com/attachments/article/483/Peskin,%20Schroesder%20-%20An%20introduction%20To%20Quantum%20Field%20Theory(T).pdf)
- [36] R. Averbeck et al. (ALICE Collaboration). “Measurement of electrons from beauty hadron decays in pp collisions at  $\sqrt{s} = 7$  TeV.” arXiv preprint arXiv:1208.1902 (2012). URL: <https://arxiv.org/pdf/1208.1902.pdf>
- [37] A. Alici et al. (ALICE Collaboration). “Performance of the ALICE Time-Of-Flight detector at the LHC.” Eur. Phys. J. Plus (2013) 128: 44. URL: <https://doi.org/10.1140/epjp/i2013-13044-x>
- [38] J. Alme et al. (ALICE Collaboration). “The ALICE TPC, a large 3-dimensional tracking device with fast readout for ultra-high multiplicity events.” Nucl.Instrum.Meth. A622 (2010) 316-367 URL: <https://www.sciencedirect.com/science/article/pii/S0168900210008910?via%3Dihub>

- [39] J. Barney et al. (S $\pi$ RIT Collaboration). “A gating grid driver for time projection chambers.” arXiv preprint arXiv:1612.06708 (2015). URL: <https://arxiv.org/pdf/1612.06708.pdf>
- [40] M. Fasel. “Single-electron analysis and open charm cross section in proton-proton collisions at  $\sqrt{s} = 7$  TeV.” Dissertation (TU, Darmstadt, 2012). URL: [http://inspirehep.net/record/1296425/files/220420496\\_CERN-THESIS-2012-311.pdf](http://inspirehep.net/record/1296425/files/220420496_CERN-THESIS-2012-311.pdf)
- [41] H. Bichsel et al. (PDG). “PASSAGE OF PARTICLES THROUGH MATTER.” (2018). URL: <http://pdg.lbl.gov/2018/reviews/rpp2018-rev-passage-particles-matter.pdf>
- [42] M. Arslanok, Physikalisches Institut, Im Neuenheimer Feld 226, 69120 Heidelberg, Germany
- [43] X. Wang et al. “HIJING: A Monte Carlo model for multiple jet production in pp, pA, and AA collisions.” Phys. Rev. Lett. D 44, 10.1103 3501-3516 (1991). URL: <https://journals.aps.org/prd/pdf/10.1103/PhysRevD.44.3501>
- [44] N. Desai et al. “An Introduction to PYTHIA 8.2.” arXiv preprint arXiv:1410.3012 (2014). URL: <https://arxiv.org/pdf/1410.3012.pdf>
- [45] B. Hess. “Particle Identification in Jets and High-Multiplicity pp Events with the ALICE TPC.” Dissertation (Uni Tübingen, 2015). URL: [http://inspirehep.net/record/1429564/files/fulltext\\_Nzyd19.pdf](http://inspirehep.net/record/1429564/files/fulltext_Nzyd19.pdf)
- [46] L. Altenkämpfer et al. “Applicability of transverse mass scaling in hadronic collisions at the LHC.” arXiv preprint arXiv:1710.01933 (2018). URL: <https://arxiv.org/pdf/1710.01933.pdf>
- [47] J. Adam et al. (ALICE Collaboration). “Multiplicity dependence of charged pion, kaon, and (anti)proton production at large transverse momentum in p–Pb collisions at  $\sqrt{s_{NN}}=5.02$  TeV.” Phys.Lett. B760 (2016) 720-735. URL: <https://arxiv.org/pdf/1601.03658.pdf>
- [48] J. Cleymans et al. “Relativistic Thermodynamics: Transverse Momentum Distribution in High-Energy Physics.” arXiv preprint arXiv:1203.4343 (2012). URL: <https://arxiv.org/pdf/1203.4343.pdf>
- [49] Y. Pachmayer et al. (ALICE Collaboration). “Measurement of electrons from beauty-hadron decays in p-Pb collisions at  $\sqrt{s_{NN}}=5.02$  TeV with ALICE at the LHC.” JHEP 1707 (2017) 052. URL: <https://link.springer.com/article/10.1007/JHEP07%282017%29052>
- [50] J. Adam et al. (ALICE Collaboration). “Multiplicity Dependence of Pion, Kaon, Proton and Lambda Production in p–Pb collisions at  $\sqrt{s_{NN}}=5.02$  TeV.” Phys.Lett. B728 (2014) 25-38. URL: <https://www.sciencedirect.com/science/article/pii/S0370269313009234?via%3Dihub>

- [51] S. Masciocchi. Interaction of particles with matter (2017). URL: [https://www.physi.uni-heidelberg.de/~sma/teaching/ParticleDetectors2/sma\\_InteractionsWithMatter\\_1.pdf](https://www.physi.uni-heidelberg.de/~sma/teaching/ParticleDetectors2/sma_InteractionsWithMatter_1.pdf)

## 10 Acknowledgment

First and foremost, I would like to thank Priv. Doz. Dr. Yvonne C. Pachmayer for not only helpful supervision but also for her endless patience with my questions and her multifaceted advice. Her patience with me becoming acquainted with the topic and root was highly appreciated. In addition I would like to thank Minjung Kim for the enduring support with coding and assisting with multiple explanations. I also express my gratitude to Dr. Alice Ohlson whose precise corrections and critics, colored in motivating green, of my writing were very helpful and a great support. Furthermore, I would like to thank the ALICE group at the PI in Heidelberg for the smart ideas, friendly advice, enduring support and the multiple tasty cakes.

# Erklärung

Ich versichere, dass ich diese Arbeit selbstständig verfasst und keine anderen als die angegebenen Quellen und Hilfsmittel benutzt habe.

Heidelberg, den .....